ACCSCIENCE PUBLISHING

International Journal of Bioprinting

RESEARCH ARTICLE

Selective laser melted Fe–30Mn–6Cu alloy: A multifunctional candidate for MRI-compatible, biodegradable, antibacterial, and biocompatible orthopedic implants

Xinjun Yang[1,2], Xinhong Yin[3], Yali He[1], Junjie Cheng[1], Xin Li[2], Guanping Chen[1], Yingchao Zhao[1], and Ming-Chun Zhao[2]*

[1]Gynecology and Obstetrics and Reproductive Medical Center, The First Affiliated Hospital, Hengyang Medical School, University of South China, Hengyang, Hunan, China

[2]School of Materials Science and Engineering, Central South University, Changsha, Hunan, China

[3]School of Nursing, University of South China, Hengyang, Hunan, China

Abstract

The orthopedic potential of biodegradable iron (Fe)–manganese (Mn)–copper (Cu) alloys remains insufficiently defined, necessitating comprehensive investigation into their mechanical properties, wear resistance, magnetic resonance imaging compatibility, biodegradation behavior, antibacterial efficacy, cytocompatibility, and osteogenic differentiation capacity. This study systematically addresses these aspects through microstructural characterization, mechanical testing, and biological evaluations of Fe–30Mn–6Cu alloy fabricated via selective laser melting (SLM). For comparison, a Cu-free Fe–30Mn alloy was fabricated under similar SLM conditions. The incorporation of 6 wt.% Cu into Fe–30Mn stabilized the γ-austenite phase, enhanced yield strength, improved wear resistance, accelerated electrochemical biodegradation, and imparted strong antibacterial activity. The SLMed Fe–30Mn–6Cu (i) exhibited a fully γ-austenite microstructure with fine equiaxed grains (~7 μm) containing Cu-enriched intergranular second-phase particles; (ii) demonstrated a yield strength of ~230 MPa—approximately ~24% higher than that of SLMed Fe–30Mn—along with improved tribological performance, a reduced hysteresis loop area indicating extremely low saturation magnetization and magnetic susceptibility, and a biodegradation rate three times higher compared to the Cu-free counterpart; and (iii) achieved a bacteriostatic rate exceeding 99% against *Escherichia coli* and *Staphylococcus aureus*, alongside excellent cytocompatibility and promotion of osteogenic differentiation in MC3T3-E1 cells. These findings provide insights into the structure–property–function relationship of multifunctional Fe–Mn–Cu alloys and their promising applicability in orthopedic implants.

Keywords: Antibacterial activity; Biodegradation; Fe–Mn–Cu alloys; Magnetic resonance imaging compatibility; Osteogenic differentiation; Tribological performance

***Corresponding author:**
Ming-Chun Zhao
(mczhao@csu.edu.cn)

Citation: Yang X, Yin X, He Y, *et al.* Selective laser melted Fe–30Mn–6Cu alloy: A multifunctional candidate for MRI-compatible, biodegradable, antibacterial, and biocompatible orthopedic implants. *Int J Bioprint.* 2025;11(3):358-380. doi: 10.36922/IJB025150128

Received: March 8, 2025
Revised: April 8, 2025
Accepted: April 9, 2025
Published online: April 11, 2025

1. Introduction

The loss or failure of bone tissue represents one of the most prevalent, debilitating, and costly challenges in human healthcare.[1] Iron (Fe)-based alloys have emerged as promising candidates for biodegradable bone implants due to their excellent physicomechanical properties and biocompatibility in physiological environments.[2–4] However, their primary limitation lies in their extremely slow degradation rate. For example, Fe-based struts remained almost intact after 53 months of implantation in a porcine model,[5] which is a concern for temporary orthopedic applications. Consequently, considerable research has focused on accelerating the degradation of Fe-based alloys.[6–8]

Another limitation of conventional Fe-based alloys is their intrinsic ferromagnetism, which is incompatible with magnetic resonance imaging (MRI).[9–11] This incompatibility results in significant imaging artifacts in MRI images caused by local magnetic field distortion, rendering the stent and vascular lumen indistinct and complicating the assessment of in-stent restenosis or the acquisition of quantitative intravascular imaging. Therefore, developing MRI-compatible Fe-based alloys is of particular importance for biomedical applications such as stents and implants. Furthermore, implant-associated infections pose a serious clinical risk. These infections can occur not only during the initial implantation stage but also throughout the implant's functional lifespan.[12] Fe-based alloys, like other metallic implants, are susceptible to such infections, limiting their broader clinical application.[13] Current treatment options, such as surgical removal of infected implants or long-term antibiotic therapy, are time-consuming and costly. Consequently, there is a strong need for Fe-based alloys with intrinsic antibacterial properties.

Wear is another critical concern, resulting from the inevitable mechanical interaction between the metallic implants and surrounding tissues. Poor wear resistance may lead to implant loosening and eventual failure.[14,15] Therefore, improving the wear resistance of Fe-based alloys is essential to ensure their long-term stability and functionality in orthopedic applications.

In light of these challenges, Fe–manganese (Mn)–copper (Cu) alloys have gained attention as potential solutions. Specifically, (i) Mn alloying can increase degradation rates while promoting the formation of antiferromagnetic γ-austenite (face-centered cubic [FCC]) or ε-martensite (hexagonal close-packed [HCP]) phases,[16–18] and (ii) Cu alloying can impart antibacterial properties while enhancing mechanical strength and wear resistance.[15,19,20] However, research on structure–property–function integrated Fe–Mn–Cu alloys—particularly those designed to simultaneously balance mechanical strength, wear resistance, MRI compatibility, biodegradation rate, antibacterial efficacy, cytocompatibility, and osteogenic differentiation potential—remain scarce. At present, there is limited mechanistic understanding of the factors governing mechanical strength, tribological performance, antiferromagnetic properties, biodegradation behavior, antibacterial activity, and biocompatibility of Fe–Mn–Cu alloys.

In this work, a Fe–Mn–Cu alloy was fabricated using 30 wt.% Mn, 6 wt.% Cu, and balance Fe powders via selective laser melting (SLM). The resulting alloy was systematically characterized in terms of microstructure, mechanical strength, wear resistance, antiferromagnetic behavior, biodegradation, antibacterial activity, cytocompatibility, and osteogenic differentiation potential. This study provides both experimental and theoretical insights into the development of structure–performance–function integrated multifunctional Fe-based alloys for orthopedic applications.

2. Materials and methods

2.1. Material preparation

Fe powders (99.99% purity, particle size: 50–75 μm), Mn powders (99.99% purity, particle size: ~50 μm), and Cu powders (99.99% purity, particle size: ~50 μm) were obtained from Changsha Tid Metal Materials Co. Ltd. (China). A mixture containing 30 wt.% Mn and 6 wt.% Cu was mechanically blended with balance Fe powder via ball milling at 300 rpm under a protective atmosphere (1 vol.% SF_6 balanced with CO_2) for 1 h. The mixed powders were then processed via SLM to fabricate Fe–30Mn–6Cu alloy (dimensions: 40 × 40 × 40 mm^3) using a self-regulating SLM system in a high-purity argon chamber. The resulting material is hereafter referred to as SLMed Fe–30Mn–6Cu. Detailed processing parameters are available in previous reports.[13,21,22] For comparison, a Cu-free Fe–30Mn alloy was prepared under identical SLM conditions by blending 30 wt.% Mn powder with balance Fe powder and is hereafter designated as SLMed Fe–30Mn.

2.2. Microstructural and mechanical characterization

The microstructure was characterized using optical microscopy (OM; Leica DMI300M, Germany) and scanning electron microscope (SEM) equipped with energy-dispersive spectrometry (EDS) (ZEI EVO-18, Germany). Samples were ground with silicon carbide (SiC) emery papers (CAIHONG, China) up to 2000 grit, mirror-polished using 1.5 μm diamond paste (HENGYU, China), ultrasonically cleaned with ethanol, and etched with a 4% nitric acid solution for ~10 s. Constituent phase analysis was performed via X-ray diffractometry (XRD; D/max 2550, Japan) using Cu Kα radiation at 40 kV and 30 mA (scan rate: 8°/min) and via X-ray photoelectron spectroscopy (XPS; Shimadzu SSL, Japan). Compression testing was conducted in triplicate using an electronic universal testing machine (Shimazu AG-Xplus, Japan) in accordance with ISO 13314 (2011). Tests were conducted at a crosshead speed of 2.5 mm/min under a maximum load of 100 kN. Cylindrical specimens (8 mm diameter × 15 mm height) were machined to ensure parallel end faces within a tolerance of ±0.02 mm.

2.3. Wear testing

Wear behavior was evaluated using a reciprocating spherical sliding wear tester (Rtec Instruments MFT-5000, USA). The samples (20 mm diameter × 6 mm height) were ground with SiC sandpaper up to 2000 grit, polished with Cr_2O_3 abrasive, cleaned in an ultrasonic cleaner with acetone, and oven-dried. Wear tests were conducted under a normal load of 5 N for 20 min in dry air at room temperature. Si_3N_4 ceramic balls were used as the counterbody. The coefficient of friction (COF) was evaluated using a computer-integrated data acquisition system (Rtec Instruments MFT-5000, USA). Wear tracks were measured using a scratch tester (MT-500, China) to determine wear loss. All experiments were repeated three times to calculate the average values.

2.4. Measurement of magnetic susceptibility

The magnetic hysteresis loop was measured at room temperature using a vibrating sample magnetometer (VSM, Lake Shore, Model 7404, USA) over a field range of ±20,000 Oe. The results were analyzed to determine the saturation magnetization (Ms), remanent magnetization, coercivity, and magnetic susceptibility.

2.5. Biodegradation testing

Biodegradation behavior was evaluated using both electrochemical and immersion tests, performed at room temperature in Hank's solution (pH = 7.4; Biosharp, China). The solution composition included 8 g/L NaCl, 0.4 g/L KCl, 0.1 g/L $MgCl_2·6H_2O$, 0.35 g/L $NaHCO_3$, 0.1 g/L $MgSO_4·7H_2O$, 0.14 g/L $CaCl_2$, 0.12 g/L $Na_2HPO_4·12H_2O$, 0.06 g/L KH_2PO_4, and 1 g/L glucose.[23]

Potentiodynamic polarization tests were performed using an electrochemical workstation (Zahner, IM6ex, Germany) at a scan rate of 1 mV/s. The sample served as the working electrode, a platinum sheet as the counter electrode, and a saturated calomel electrode (SCE) as the reference electrode. All potentials were reported relative to the SCE. The potential was scanned from −0.8 to 0.5 V versus the open-circuit potential (OCP), after stabilization. Electrochemical impedance spectroscopy (EIS) measurements were conducted at the stabilized OCP over a frequency range from 100 kHz to 10 MHz. Data were analyzed using ZSimWin software (AMETEK, USA).

For both electrochemical tests, samples were encapsulated in epoxy resin, exposing a 10 × 10 mm^2 surface area to 500 mL of Hank's solution. Prior to testing, the exposed surface was grounded with 1200-grit SiC paper and rinsed with distilled water. The electrochemical biodegradation rate (P_i, in mm/year) was calculated using **Equations (I) and (II)**[24,25]:

$$P_i = K \cdot \frac{i_{corr}}{\rho} \cdot E_w \quad \text{(I)}$$

$$E_w = \frac{1}{\Sigma \frac{n_i f_i}{w_i}} \quad \text{(II)}$$

where K is a constant (3.27×10^{-3} mm·g/A/cm/year); ρ is the density (g/cm^3); E_w is the electrochemical equivalent; n_i, f_i, and w_i represent the valence, mass fraction, and atomic weight of the i-th element, respectively.

For the immersion testing, specimens were also encapsulated in epoxy resin with a single exposed surface (dimensions: 10 × 10 mm^2) submerged in Hank's solution for 28 days. The solution was refreshed every 24 h. Prior to immersion, surfaces were polished to 1200 grit using SiC abrasive paper, rinsed with distilled water, and dried using warm flowing air. The immersion biodegradation rate (P_w, in mm/year) was calculated using **Equation (III)**[13]:

$$P_w = \frac{K \times \left(W_a - W_b\right)}{A\rho T} \quad \text{(III)}$$

where K is 8.76×10^4, W_a is the initial mass (g) of the specimen, W_b is the mass (g) of the specimen after the immersion test, A is the exposed surface area of the specimen (cm^2), T is the immersion time (h), and ρ is the material density (g/cm^3). Each immersion test was conducted in triplicate. After immersion, corrosion morphologies were characterized using SEM.

2.6. Antibacterial properties

The antibacterial activity of the samples was evaluated using the colony counting method using *Escherichia coli* and *Staphylococcus aureus*. Test samples were mechanically polished, sterilized by high-temperature autoclaving, and immersed in sterile phosphate-buffered saline (PBS) at a surface area-to-volume ratio of 1.25 cm^2/mL. After incubation at 37°C for 48 h, the solution was filtered through a 0.25 μm membrane to obtain metal extracts. The extracts were co-incubated with *E. coli* and *S. aureus* at an initial concentration of 1×10^5 CFU/mL at 37°C for 24 h. For the experimental group, 100 μL of the metal extract was mixed with 100 μL of bacterial suspension. In the control group, 100 μL of sterile PBS was mixed with 100 μL of bacterial suspension. After incubation, 100 μL from each group was spread onto agar plates and incubated for an additional 24 h. The number of viable bacterial colonies was then counted, and the antibacterial rate (K) was calculated using **Equation (IV)**[26,27]:

$$K = \frac{\alpha_0 - \alpha_t}{\alpha_0} \times 100\% \tag{IV}$$

where α_0 and α_t are the number of bacterial colonies in the control and experimental group, respectively. Each test was performed in triplicate.

2.7. Cytocompatibility and osteogenic differentiation

The biocompatibility and osteogenic differentiation potential of the metal extracts were assessed using the following methods: CCK-8 cell proliferation, Live/Dead staining, alkaline phosphatase (ALP) activity, and alizarin red S (ARS) staining. All experiments were conducted using MC3T3-E1 pre-osteoblast cells (Cell Cook, Guangzhou, China).

Test samples were mechanically polished and sterilized using high-temperature autoclaving. The sterilized samples were immersed in sterile PBS at a surface area-to-volume ratio of 1.25 cm^2/mL and incubated at 37 °C for 48 h. The resulting extracts were filtered through a 0.22 μm membrane and used for subsequent biological assays.

MC3T3-E1 cells were cultured in α-MEM supplemented with 10% fetal bovine serum and 1% penicillin-streptomycin in a humidified incubator at 37 °C with 5% CO_2. The culture medium was refreshed every 2 days. For CCK-8 and Live/Dead staining assays, cells were seeded in 96-well plates at a density of 5×10^4 cells/mL (100 μL per well). For osteogenic differentiation assays, cells were seeded in 24-well plates at 1×10^5 cells/mL (500 μL per well). After allowing cells to adhere for 24 h, the experimental group was treated with 100 μL of metal extract, while the control group received 100 μL of α-MEM medium.

Biocompatibility assays were conducted after 1 and 3 days of incubation, while osteogenic differentiation assays were performed on Days 7 and 14. For cell viability assessment, 10 μL CCK-8 reagent (Beytime, China) was added to each well, followed by a 2-h incubation at 37 °C. Absorbance at 450 nm was measured using a microplate reader, and relative cell viability was calculated as a percentage of the control group.

Live/Dead staining was performed in parallel. After 1 and 3 days, cells were washed three times with PBS and incubated with a staining solution containing Calcein-AM (for live cells) and propidium iodide (PI; for dead cells) for 30 min at 37°C in the dark. Fluorescence microscopy (OLYMPUS, IXplotm^{TM} IX85, Japan) was used to visualize cell viability: viable cells fluoresced green (Calcein-AM), while non-viable cells fluoresced red (PI).

For osteogenic differentiation, ALP activity and ARS staining were conducted on Days 7 and 14. For ALP staining, cells were washed with PBS, fixed with 4% paraformaldehyde for 15 min at room temperature, and stained with BCIP/NBT staining solution (Beytime, China) at 37 °C for 30 min. Purple-blue precipitates indicated ALP enzymatic activity, a marker of early osteogenic differentiation. ARS staining was performed to assess calcium mineralization. Cells were washed with PBS, fixed with 4% paraformaldehyde for 15 min, and stained with 40 mM ARS (pH 4.2) for 30 min. Excess dye was removed by thorough rinsing with PBS. Red-stained calcium deposits were observed under a light microscope and quantified to evaluate the extent of mineralization and osteogenic differentiation.

2.8. Statistical analysis

To ensure the reliability of the experimental results, all tests—mechanical properties, COF, electrochemical corrosion behavior, and cell compatibility—were performed in parallel. Data are presented as mean ± standard deviation. Statistical comparisons were conducted using one-way analysis of variance (ANOVA), with a significance threshold of $p < 0.05$.

3. Results

3.1. Microstructure

Figure 1 shows the OM and SEM images of SLMed Fe–30Mn–6Cu. As shown in Figure 1a, the OM image reveals a relatively compact matrix with fine equiaxed grains, exhibiting an average grain size of ~7 μm. In Figure 1b, the SEM image demonstrates a microstructure composed primarily of gray equiaxed grains interspersed with white second-phase particles, which are predominantly distributed along the grain boundaries.

Figure 2 presents the SEM-EDS analysis of SLMed Fe–30Mn–6Cu, highlighting the compositional distributions within the second-phase particles and matrix grains.

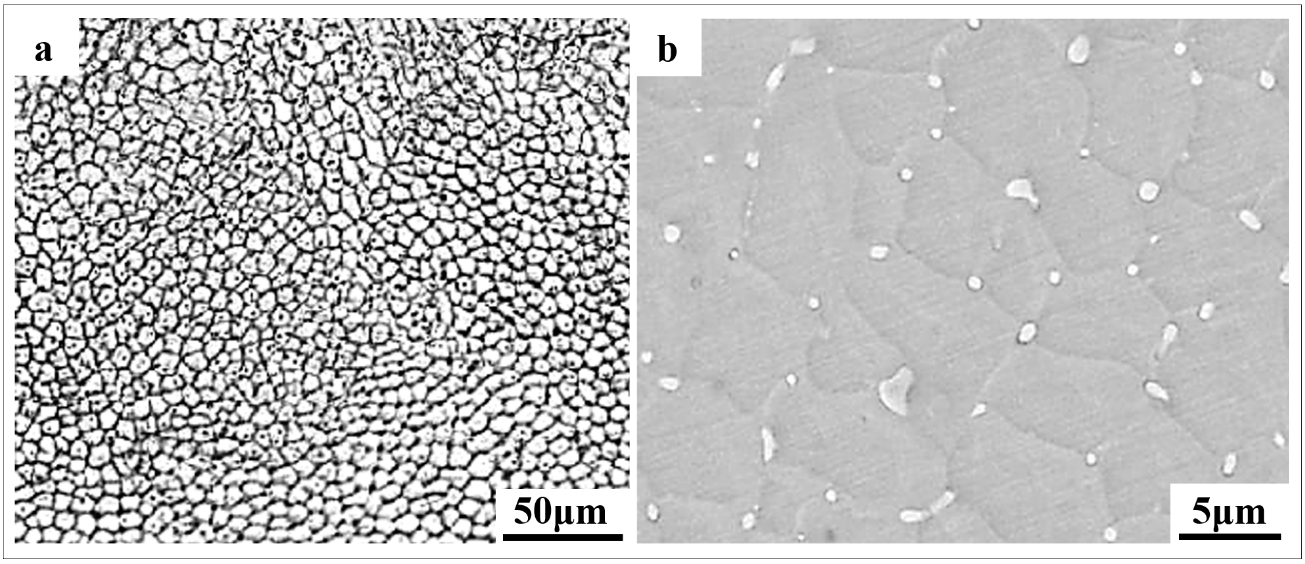

Figure 1. Microscopic images of SLMed Fe–30Mn–6Cu. (a) Optical microscopy; scale bar: 50 μm, magnification: 1000×. (b) Scanning electron microscopy; scale bar: 5 μm, magnification: 10 000×.

The compositions were evaluated using EDS spectra, as illustrated in Figure 2b and c. At least three points were analyzed in each representative region. Although EDS is not a highly precise compositional tool, its semi-quantitative results provide an estimation of the compositional distribution within the microstructure. Points 1 and 2 in Figure 2a correspond to a second-phase particle and a matrix grain, respectively. Point 1 exhibited a Cu content of 51.3 at.%, while Point 2 contained 5.5 at.% Cu. This indicates that the intergranular second-phase particles are significantly enriched in Cu compared to the matrix. The presence of 5.5 at.% Cu in the matrix grains indicates only limited Cu solubility within the Fe–Mn matrix.

The corresponding EDS elemental maps of Fe, Mn, and Cu (Figure 2d–f) further confirm the elemental distribution. In these maps, green, red, and light blue represent Fe, Mn, and Cu, respectively. Fe and Mn are uniformly dispersed throughout the matrix, whereas Cu is predominantly localized within the intergranular second-phase particles. Together, these results confirm that the intergranular second-phase particles are Cu-rich.

The formation of these Cu-enriched particles can be explained by solidification behavior. During solidification, Mn preferentially dissolves into the Fe matrix, forming a high-Mn solid solution that stabilizes the γ-austenite phase.[28,29] Meanwhile, Cu is rejected into the remaining liquid phase at the advancing solid–liquid interface, facilitating the nucleation of Cu-rich phase particles along the periphery of the growing γ-austenite grains. As a result, Cu-rich second-phase particles accumulate along grain boundaries.

Figure 3a shows the XRD patterns of SLMed Fe–30Mn–6Cu compared with SLMed Fe–30Mn. Based on the standard powder diffraction file card (Reference code: 52-0513, 34-0529) and the Fe–Mn binary phase diagram,[30] Cu exhibits limited solid solubility in Fe. The primary diffraction peaks of SLMed Fe–30Mn correspond to the γ-austenite phase with an FCC structure and the ε-martensite phase with an HCP structure. In contrast, SLMed Fe–30Mn–6Cu exhibits dominant peaks corresponding to the γ-austenite phase (FCC structure), suggesting that the addition of 6 wt.% Cu stabilizes the γ-austenite phase while suppressing the formation of other phases. The absence of detectable Cu-rich phases in the XRD pattern is likely due to their low volume fraction.

Figure 3b presents the XPS survey spectrum of SLMed Fe–30Mn–6Cu, confirming the presence of Fe, Mn, Cu, and oxygen (O) on the surface. The high-resolution Fe spectrum (Figure 3b$_1$) reveals peaks corresponding to both metallic Fe (Fe^0) and oxidized states (Fe^{2+} and Fe^{3+}). The Fe^{3+} peaks centered at ~724.0 eV correspond to Fe_2O_3, likely formed due to oxidation under ambient conditions, while the Fe^{2+} peak at ~710.3 eV indicates the presence of FeO. The high-resolution Mn spectrum (Figure 3b$_2$) shows Mn predominantly in the Mn^{2+} oxidation state (MnO), with a peak at ~640.5 eV. A minor metallic Mn^0 signal at ~640.9 eV suggests partial oxidation. The absence of higher oxidation states (e.g., Mn^{3+}/Mn^{4+}) indicates the relative stability of Mn^{2+}. The high-resolution Cu spectrum (Figure 3b$_3$) shows that Cu exists in both metallic (Cu^0, ~932.5 eV) and oxidized (Cu^{2+}, ~952.7 eV, corresponding to CuO) states.

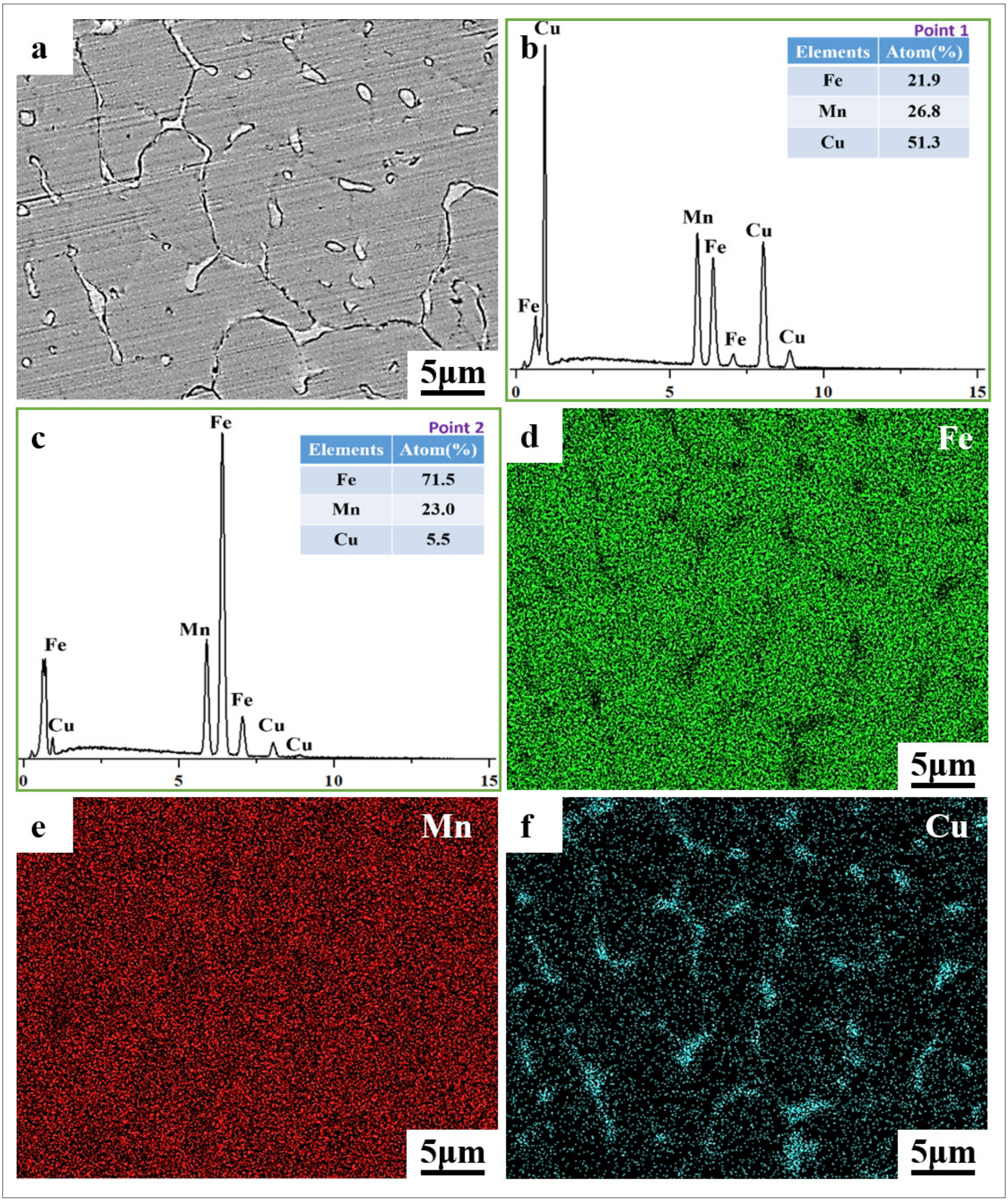

Point 1

Elements	Atom(%)
Fe	21.9
Mn	26.8
Cu	51.3

Point 2

Elements	Atom(%)
Fe	71.5
Mn	23.0
Cu	5.5

Figure 2. Scanning electron microscopy coupled with energy-dispersive X-ray spectroscopy (SEM-EDS) analysis of SLMed Fe–30Mn–6Cu: (a) SEM image; scale bar: 5μm; magnification: 10,000x. (b, c) EDS spectra of Points 1 and 2 in (a). (d–f) EDS elemental maps of Fe, Mn, and Cu, respectively, in (a).

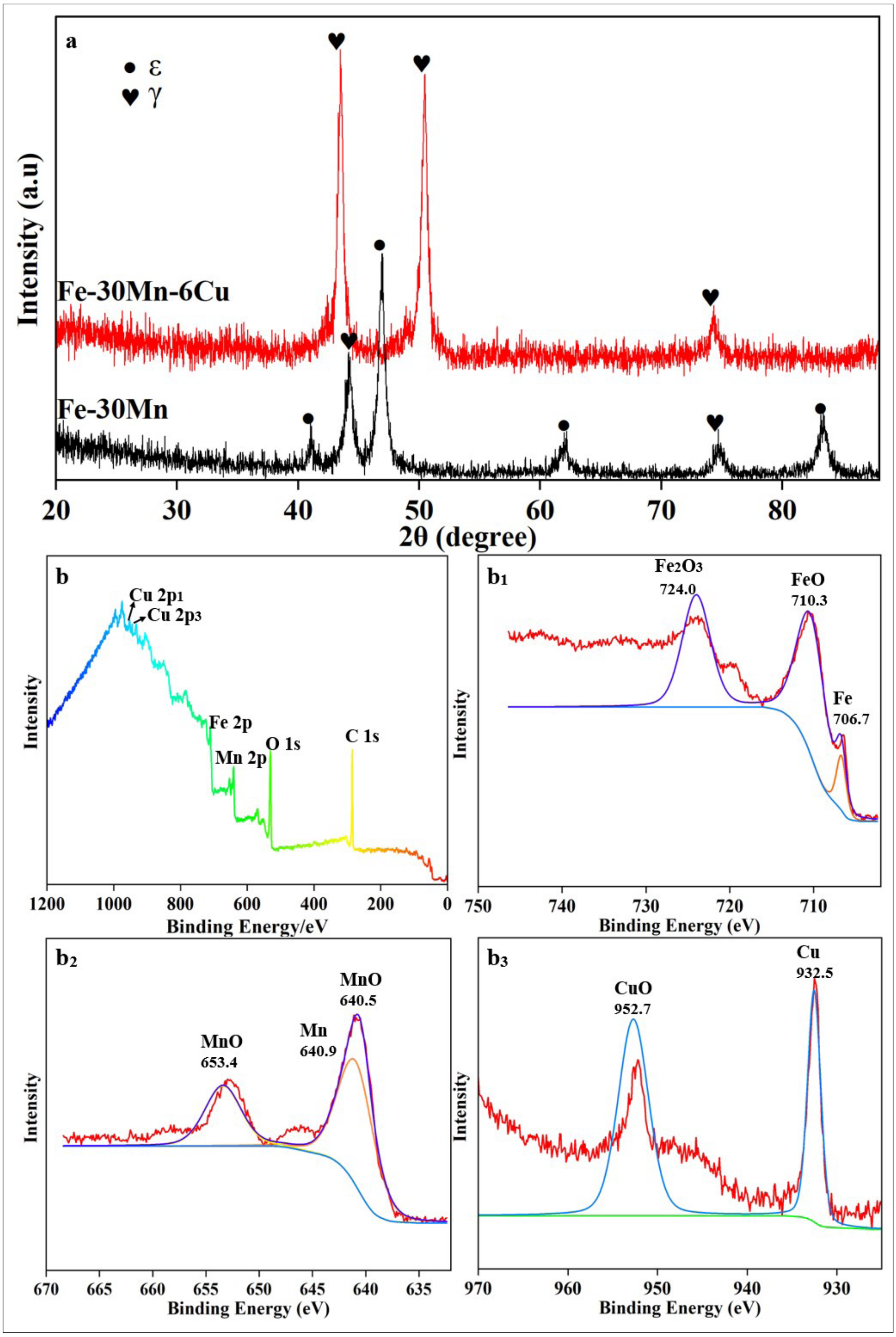

Figure 3. X-ray diffractometry (XRD) and X-ray photoelectron spectroscopy (XPS) analysis of SLMed Fe–30Mn–6Cu: (a) XRD pattern. (b) XPS survey spectrum; (b_1, b_2, b_3) high-resolution spectra of Fe, Mn, and Cu, respectively.

3.2. Mechanical and tribological properties

Figure 4a shows the compressive stress–strain curves of SLMed Fe–30Mn–6Cu and SLMed Fe–30Mn, while the corresponding yield strength (YS) and elastic modulus (*E*) are summarized in Figure 4b. The YS of SLMed Fe–30Mn reached ~185 MPa, significantly higher than that of conventionally sintered Fe–30Mn (~137 MPa).[31] This improvement is attributed to the pronounced grain refinement induced by the rapid solidification associated with the SLM process.[32,33] Alloying Cu into Fe–30Mn further improved the YS, with SLMed Fe–30Mn–6Cu achieving ~300 MPa—a ~62.2% increase over SLMed Fe–30Mn. The *E* increased from ~4 GPa in SLMed Fe–30Mn to ~7 GPa in SLMed Fe–30Mn–6Cu. Both values fall within the range of human weight-bearing bones, which is beneficial for reducing stress shielding in orthopedic applications.[34–36]

Figure 5a displays the COF curves of SLMed Fe–30Mn–6Cu and SLMed Fe–30Mn. The COF curve of SLMed Fe–30Mn gradually increased and stabilized between 0.8 and 0.9, with an average COF of ~0.85. In contrast, the COF curve of SLMed Fe–30Mn–6Cu exhibited a similar trend but stabilized below 0.8 with reduced fluctuation, yielding an average COF of SLMed Fe–30Mn–6Cu of ~0.8—lower than that of SLMed Fe–30Mn.

Figure 5b presents the wear track profiles. For SLMed Fe–30Mn, the wear track measured 1.3 mm in width, 17.5 µm in depth, and 0.25 mm^3 in wear volume. For SLMed Fe–30Mn–6Cu, the corresponding values were 0.91 mm in width, 8.41 µm in depth, and 0.045 mm^3 in wear volume, representing reductions of 31.6%, 52%, and 82%, respectively.

Figure 5c and d shows SEM images of the worn surfaces. Both materials exhibited plowing wear, primarily due to the significantly higher hardness of the grinding ball relative to the test samples. In Figure 5c, SLMed Fe–30Mn displayed numerous cracks, delaminations, and severe plowing, indicating dominant adhesive, fatigue, and abrasive wear mechanisms. In contrast, Figure 5d shows that SLMed Fe–30Mn–6Cu experienced only slight plowing, scattered debris, and small pits, indicating that adhesive abrasive wear was present but to a lesser degree.

The corresponding EDS data from Point 1 (Figure 5c) and Point 2 (Figure 5d) are presented in Table 1. Both points exhibited high O content, indicating the presence of oxidation wear. This phenomenon could be attributed to elevated surface temperatures during the wear test, which promoted the formation of oxide layers through the reaction of Fe with atmospheric O.

3.3. Magnetic performance

Figure 6 illustrates the magnetic hysteresis loops of SLMed Fe–30Mn–6Cu compared with SLMed Fe–30Mn. The corresponding magnetic performances are summarized in Table 2. Both alloys exhibited extremely narrow hysteresis loops, with SLMed Fe–30Mn–6Cu showing a smaller hysteresis loop area. This reflects extremely low saturation magnetization and magnetic susceptibility, indicating excellent MRI compatibility.

3.4. Biodegradation

Figure 7a presents the potential polarization curves of SLMed Fe–30Mn–6Cu and SLMed Fe–30Mn. Corrosion potential (E_{corr}) and corrosion current density (I_{corr}) were

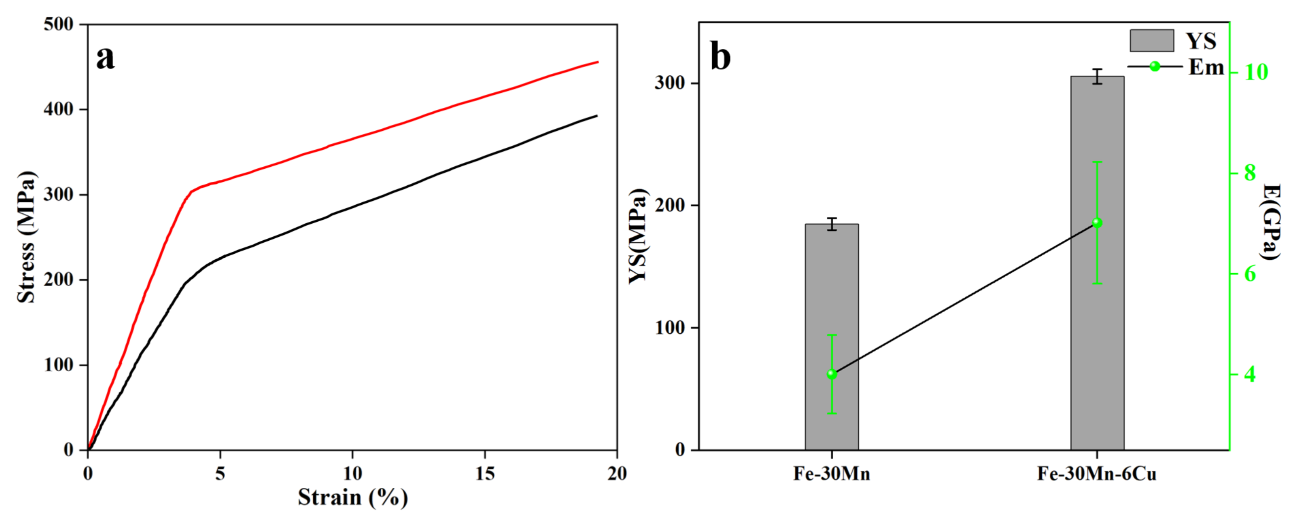

Figure 4. Mechanical properties of SLMed Fe–30Mn and Fe–30Mn–6Cu alloys. (a) Compressive stress–strain curves. (b) Yield strength (YS) and elastic modulus (*E*).

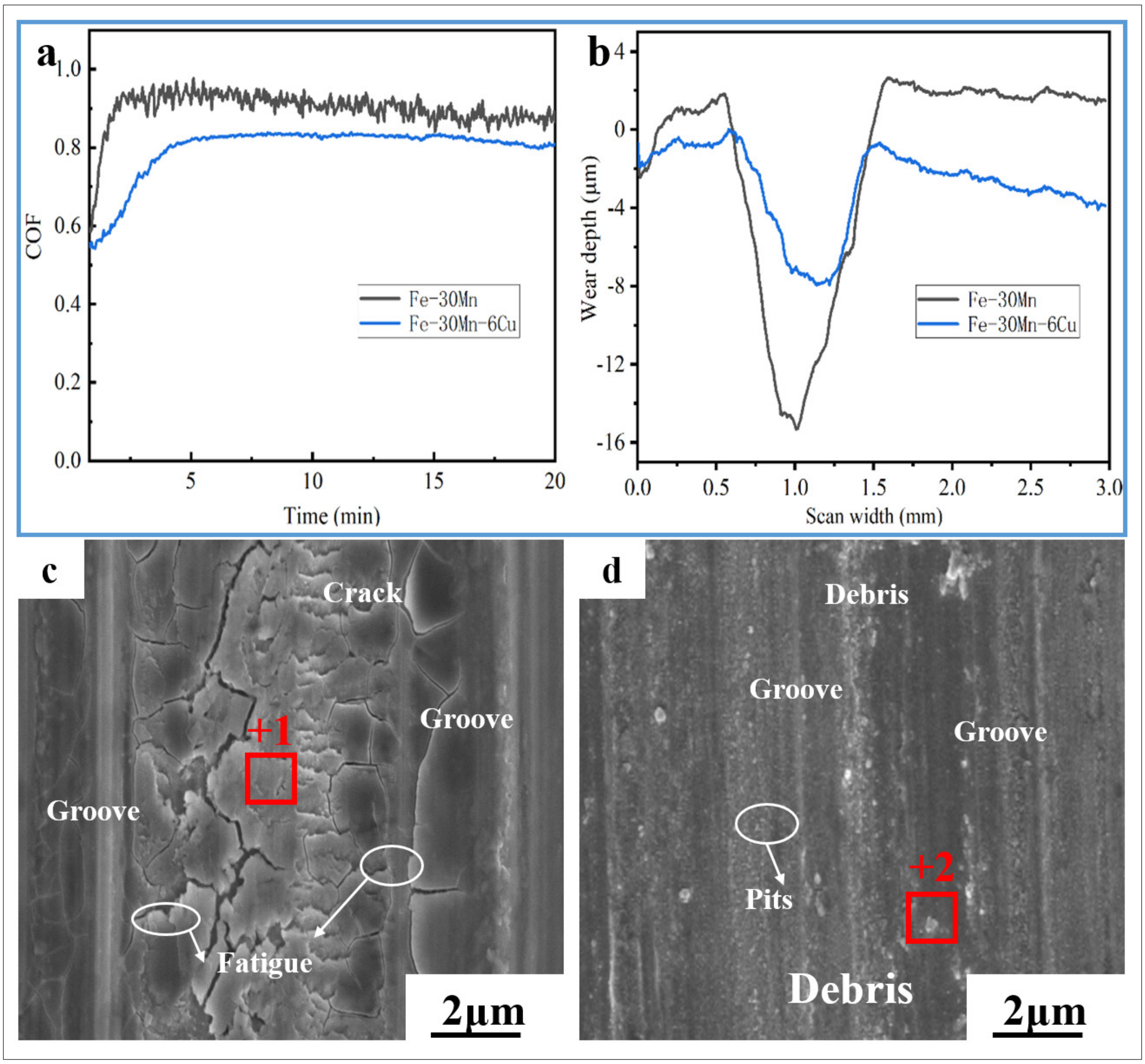

Figure 5. Tribological properties of SLMed Fe–30Mn and Fe–30Mn–6Cu alloys. (a) Coefficient of friction (COF) curves. (b) Wear track profiles, (c, d) SEM images of the worn surface of (c) SLMed Fe–30Mn (scale bar: 2 μm, magnification: 20,000×) and (d) SLMed Fe–30Mn–6Cu (scale bar: 2 μm, magnification: 20,000×).

Table 1. Energy-dispersive spectrometry profiles of worn surfaces at Point 1 (Figure 5c) and Point 2 (Figure 5d)

Alloy	Point	Fe (wt.%)	Mn (wt.%)	Cu (wt.%)	O (wt.%)
SLMed Fe–30Mn	Point 1	55.8	21.8	-	22.4
SLMed Fe–30Mn–6Cu	Point 2	58.3	18.5	6.4	16.8

Table 2. Magnetic properties of SLMed Fe–30Mn and SLMed Fe–30Mn–6Cu

Alloy	Ms (emu/g)	Mr (emu/g)	Hc (Oe)	χ (m³/kg)
SLMed Fe–30Mn	0.48	0.045	123.52	5.25×10^{-6}
SLMed Fe–30Mn–6Cu	0.18	0.006	125.33	1.33×10^{-6}

Notes: χ, magnetic susceptibility; H_c, coercivity; M_r, remanent magnetization; M_s, Saturation magnetization.

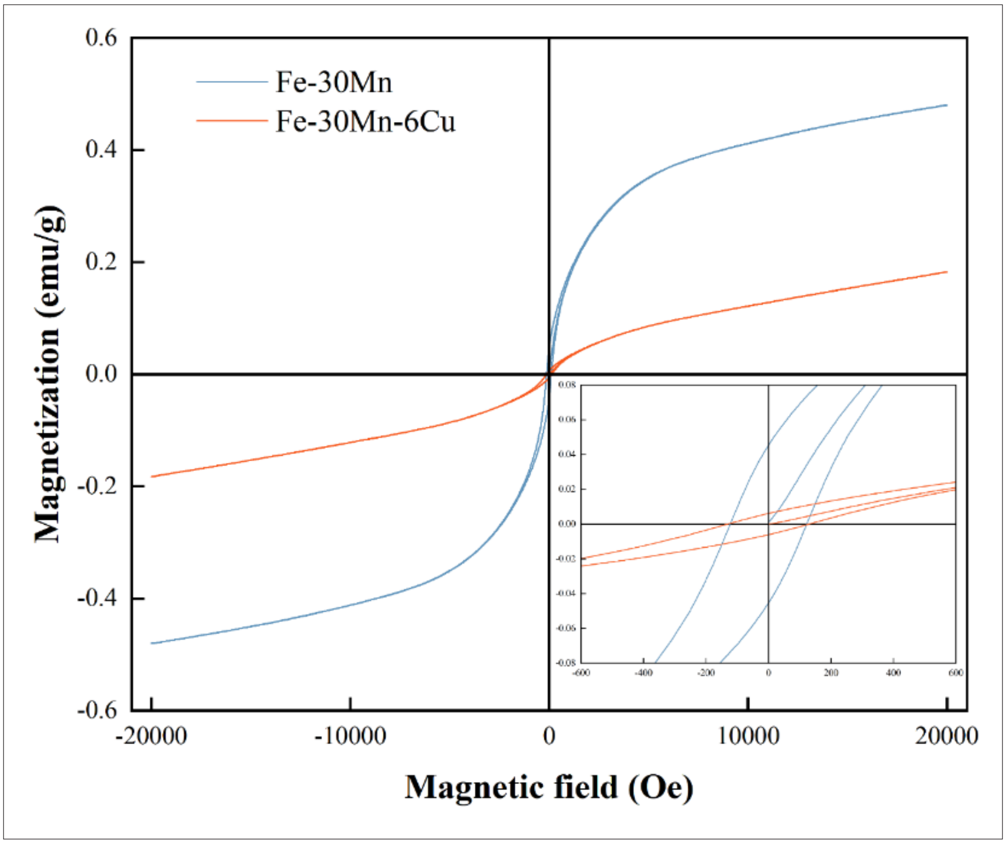

Figure 6. Magnetic hysteresis loops of SLMed Fe–30Mn and SLMed Fe–30Mn–6Cu.

determined via Tafel extrapolation, and the corresponding corrosion rate (P_i) was calculated using **Equations (I) and (II)**. Electrochemical testing revealed that SLMed Fe–30Mn–6Cu exhibited a corrosion rate approximately three times higher (2.51 mm/year) than that of SLMed Fe–30Mn (0.75 mm/year), as shown in Table 3. This acceleration is attributed to a galvanic coupling between the Cu-rich intergranular phases (anodic sites) and the γ-austenite matrix (cathodic sites). Figure 7b displays the Nyquist plots obtained from EIS. Both alloys exhibited similar curve shapes with a single capacitive loop with varying diameters in the measured frequency range. The diameter of the capacitive loop correlates with polarization resistance: a smaller diameter corresponds to lower polarization resistance and a higher corrosion rate.[37–39] The smaller capacitive arc diameter for SLMed Fe–30Mn–6Cu signifies an accelerated electrochemical process.

Mass loss-based corrosion rates (P_w) after 28 days vof immersion in Hank's solution are also listed in Table 3. SLMed Fe–30Mn–6Cu exhibited a corrosion rate of 2.4 mm/year, ~3.6 times that of SLMed Fe–30Mn (0.66 mm/year), consistent with electrochemical test results.

Figure 8 shows the corrosion morphologies and corresponding analysis of SLMed Fe–30Mn (Figure 8a, a_1, and a_2) and SLMed Fe–30Mn–6Cu (Figure 8b, b_1, and b_2) after 28 days of immersion in Hank's solution. SEM-EDS data were collected from selected points (Point 1 for Fe–30Mn and Point 2 for Fe–30Mn–6Cu) on the uncleaned surfaces (Figure 8a and b), with the corresponding spectra shown in Figure 8a_1 and b_1. Both spectra revealed the

Table 3. Electrochemical parameters of SLMed Fe–30Mn and SLMed Fe–30Mn–6Cu

Alloy	E_{corr} (V)	I_{corr} (μA/cm²)	Corrosion rate P_i (mm/year)	Corrosion rate P_w (mm/year)
SLMed Fe–30Mn	–0.68	179.8	0.75	0.66 ± 0.05
SLMed Fe–30Mn–6Cu	–0.84	598.5	2.51	2.4 ± 0.08

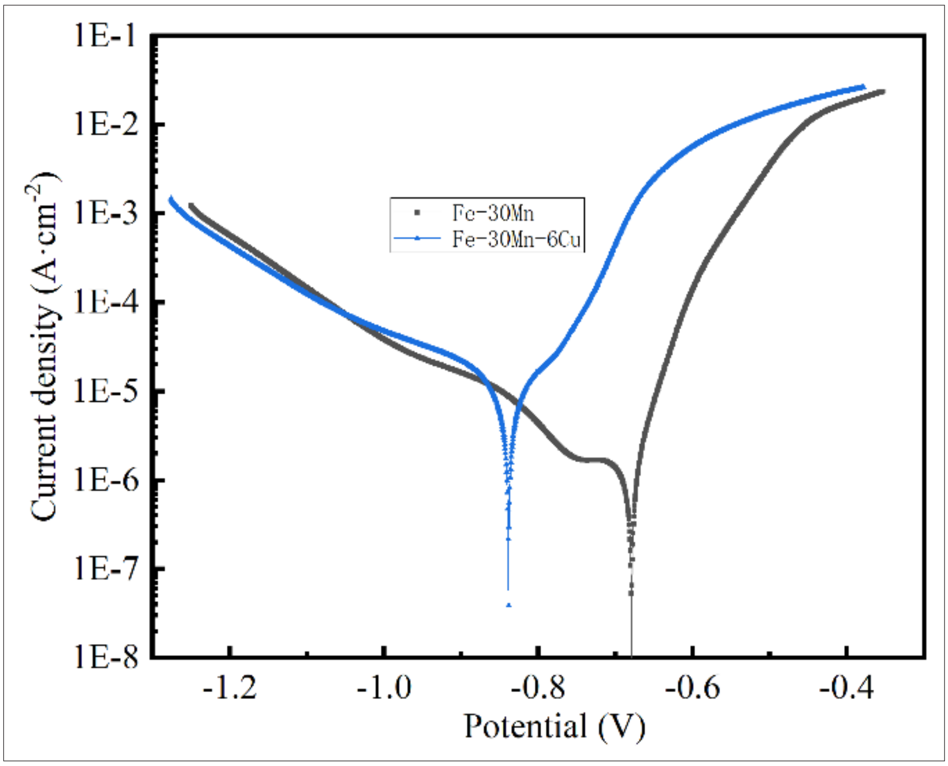

Figure 7. Electrochemical performance of SLMed Fe–30Mn and SLMed Fe–30Mn–6Cu: (a) potential polarization curves; (b) Nyquist plots.

presence of Fe, O, Ca, and P, indicating that the corrosion products likely included Fe_2O_3, $Fe(OH)_3$, and apatite. After the removal of the corrosion products, SLMed Fe–30Mn exhibited only a few shallow corrosion pits (Figure $8a_2$), whereas SLMed Fe–30Mn–6Cu displayed numerous deep pits (Figure $8b_2$). These findings indicate that the addition of 6 wt.% Cu significantly intensified corrosion, leading to accelerated degradation of the Fe–30Mn–6Cu alloy.

3.5. Antibacterial properties

Figure 9 shows macroscopic images of *E. coli* and *S. aureus* colonies after 24-h co-culture with leachates from SLMed Fe–30Mn and SLMed Fe–30Mn–6Cu leachates.

For *E. coli*, the blank group exhibited 400 ± 30 colonies. The SLMed Fe–30Mn leachate reduced the colony count to 120 ± 10, corresponding to an antibacterial rate of 70%. In contrast, the SLMed Fe–30Mn–6Cu leachate resulted in nearly zero colonies, achieving a 99.9% antibacterial rate. These results demonstrate that the SLMed Fe–30Mn–6Cu leachate possesses significantly stronger inhibitory activity against *E. coli* compared to the SLMed Fe–30Mn leachate. A similar trend was observed for *S. aureus*. While the blank group exhibited a high colony count, the SLMed Fe–30Mn leachate moderately reduced bacterial growth, and the Fe–30Mn–6Cu leachates led to a substantial reduction, indicating superior antibacterial efficacy.

3.6. Cytocompatibility and osteogenic differentiation

Figure 10a presents Live/Dead fluorescence staining images of MC3T3-E1 cells co-cultured with leachates from SLMed Fe–30Mn and SLMed Fe–30Mn–6Cu for 1 and 3 days. After 1 day, the blank group exhibited predominantly live cells (green) with no dead cells (red). Both SLMed groups also showed mostly viable cells. By Day 3, the blank group exhibited an increased number of live cells with minimal cell death, while the SLMed groups exhibited slightly higher live cell counts compared to the blank group, confirming good cytocompatibility. Figure 10b and c presents the results of the CCK-8 assay and the corresponding relative growth rate, further supporting the excellent cytocompatibility of both leachates.

Figure 11a shows ALP activity in MC3T3-E1 cells co-cultured with leachates from SLMed Fe–30Mn and SLMed Fe–30Mn–6Cu for 7 and 14 days. On day 7, ALP activity was comparable among all groups. By day 14, a slight increase was observed in the blank group, while the SLMed Fe–30Mn and Fe–30Mn–6Cu leachates induced moderate and significant increases, respectively—indicating

]

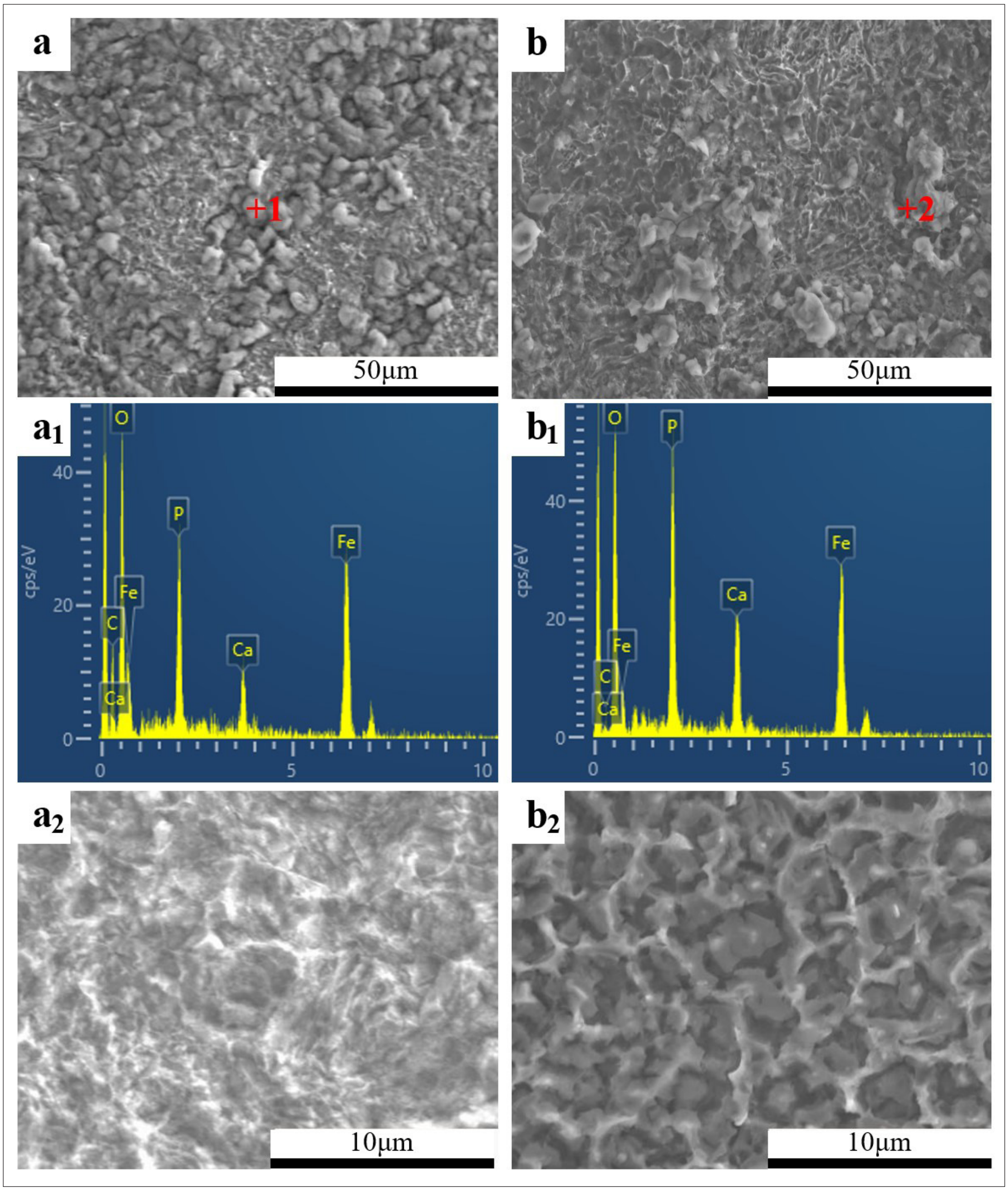

Figure 8. Scanning electron microscopic (SEM) images of uncleaned surface for (a) SLMed Fe–30Mn (scale bar: 50 μm, magnification: 1000×) and (b) SLMed Fe–30Mn–6Cu (scale bar: 50 μm, magnification: 1000×). (a_1, b_1) Energy-dispersive spectrometry spectrum of Point 1 in (a) and Point 2 in (b). (a_2, b_2) SEM images of cleaned surface for SLMed Fe–30Mn (a_2; scale bar: 50 μm, magnification: 5000×) and SLMed Fe–30Mn–6Cu (b_2; scale bar: 10 μm, magnification: 5000×).

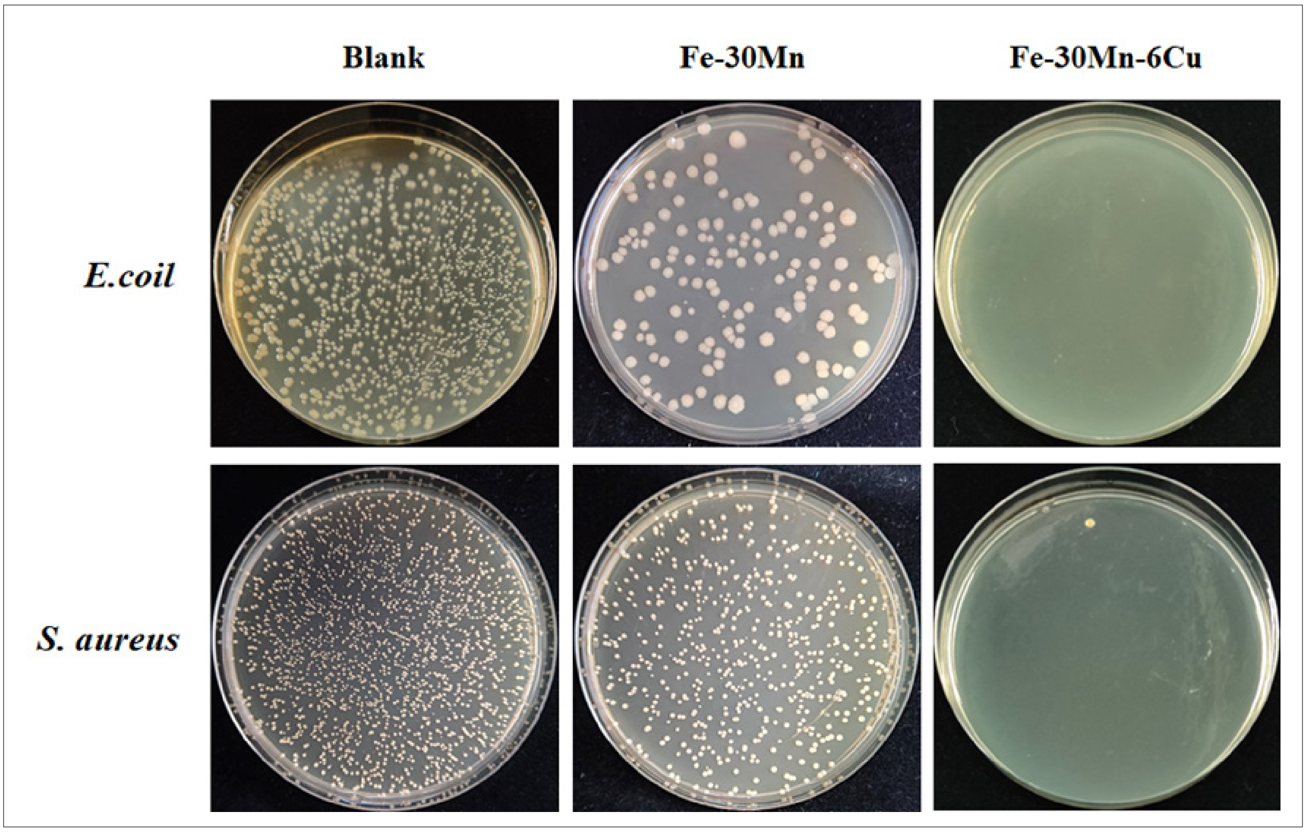

Figure 9. Macroscopic colony images of *E. coli* and *S. aureus* co-cultured with SLMed Fe–30Mn and SLMed Fe–30Mn–6Cu leachates for 24 h.

enhanced osteogenic potential in the Cu-containing alloy. Figure 11b illustrates calcium nodule formation under the same conditions. After 7 days, only a few calcium nodules were observed in the blank group and the SLMed Fe–30Mn and SLMed Fe–30Mn–6Cu leachate groups. By 14 days, the blank group exhibited a slight increase, the SLMed Fe–30Mn leachate group showed a moderate increase, and the SLMed Fe–30Mn–6Cu leachate group exhibited a marked rise in calcium nodule formation. These results confirm the promotive effect of Cu on osteogenic differentiation, with SLMed Fe–30Mn–6Cu demonstrating the highest osteogenic potential among the tested groups.

4. Discussion

4.1. Physicomechanical properties

The microstructure of Fe–30Mn has been extensively characterized and is predominantly composed of the γ-austenite phase with an FCC structure. In the present work, in addition to the γ-austenite phase (FCC structure), an ε-martensite phase (HCP structure) was also observed in SLMed Fe–30Mn. The presence of ε-martensite in SLMed Fe–30Mn is likely attributable to the unique conditions of the SLM process, which facilitates the formation of a supersaturated solid solution of metastable α-ferrite during rapid solidification.[40]

Alloying Cu into SLMed Fe–30Mn stabilized the γ-austenite phase, resulting in a single-phase γ-austenite structure in SLMed Fe–30Mn–6Cu. As a well-known austenite stabilizer, Cu expands the γ-phase field in Fe-based alloys,[41] thereby promoting the formation of a fully austenitic matrix in this alloy. Furthermore, SLMed Fe–30Mn–6Cu exhibited remarkable grain refinement, with an average grain size of ~7 μm and fine equiaxed grains, as displayed in Figure 1a. This grain size is significantly smaller than that of conventionally cast Fe–Mn alloys, which typically exhibit grain sizes ranging from tens to thousands of micrometers. The grain refinement is primarily due to the high solidification rate and supercooling inherent to the SLM process,[32,33] which enhance nucleation rates and promote multidirectional grain growth. Additionally, Cu further contributed to grain refinement through two mechanisms as follows: (i) solute Cu enrichment at the solid–liquid interface induces undercooling, reduces atomic diffusion rate, and promotes primary Fe nucleation; and (ii) dispersed Cu-rich phase particles at grain boundaries inhibit grain growth.

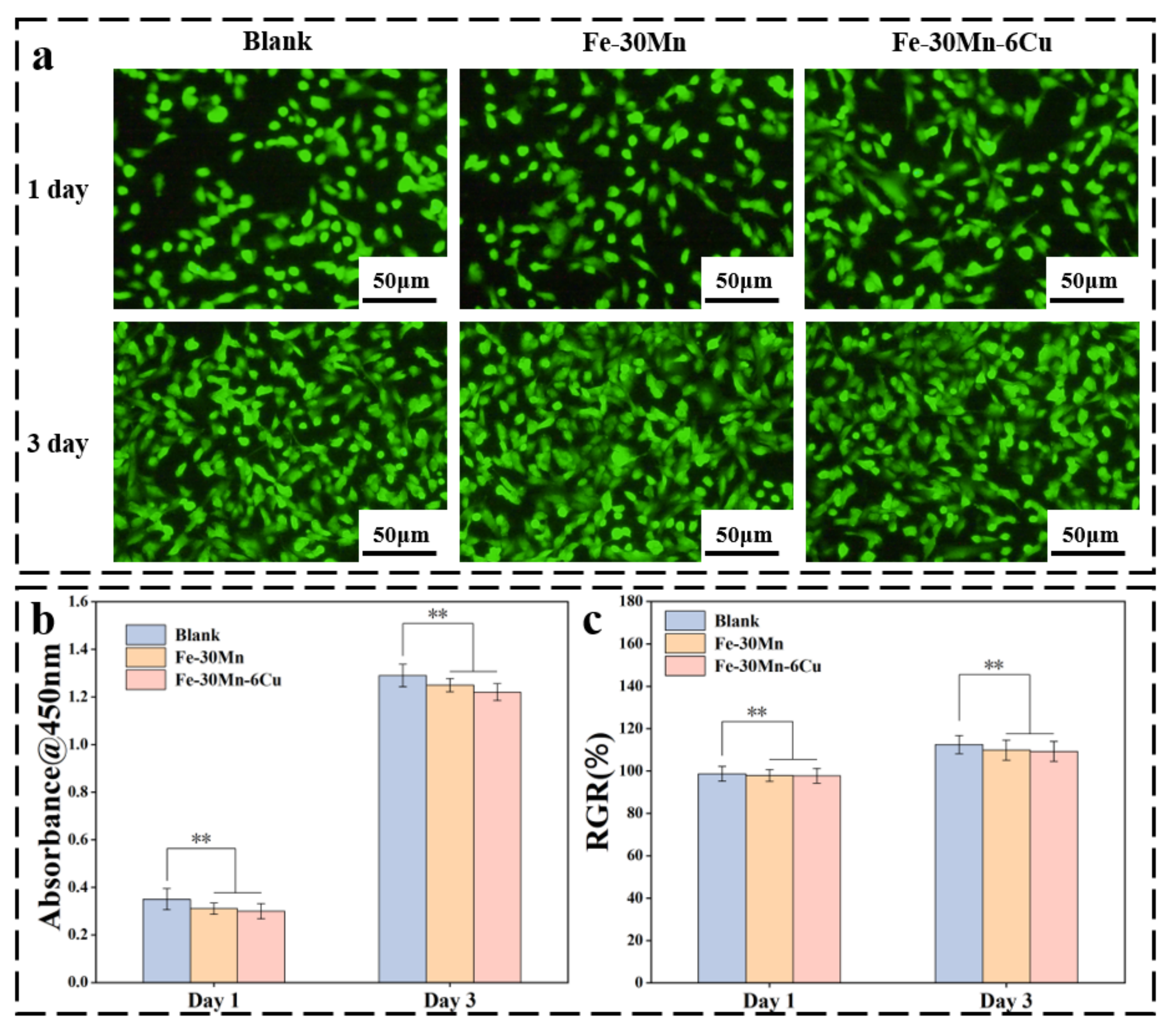

Figure 10. The cytocompatibility of leachates from SLMed Fe–30Mn and SLMed Fe–30Mn–6Cu. (a) Live/Dead fluorescence staining images of MC3T3-E1 cells after 1 and 3 days of co-cultured; scale bars: 50 μm, magnification: 20×. (b) CCK-8 assay results. (c) Relative growth rate (RGR).

For bone implant applications, compressive YS and E are critical design parameters.[42–44] SLMed Fe–30Mn exhibited a YS of ~185 MPa, significantly higher than that of sintered Fe–30Mn (~137 MPa),[31] due to grain refinement resulting from rapid solidification. This strength approaches the YS of biomedical-grade 316L stainless steel (~240 MPa).[45] Cu alloying further enhanced the YS to ~300 MPa, representing a 62.2% increase compared to SLMed Fe–30Mn without Cu. These results demonstrate that SLMed Fe–30Mn–6Cu is well-suited for high-strength biodegradable applications, such as load-bearing orthopedic implants. The improvement in strength arises from the synergistic effects of grain refinement (via rapid solidification) and the pinning action of Cu-rich particles at grain boundaries. As illustrated in Figure 2, Cu predominantly precipitates at grain boundary phases due to its low solubility in Fe/Mn matrices, thereby inhibiting grain growth and improving mechanical strength.[46] Solid solution strengthening by Cu is considered negligible due to its limited solubility.

Both SLMed Fe–30Mn and SLMed Fe–30Mn–6Cu demonstrated compressive strains of ~20%, indicating adequate ductility to accommodate post-implantation deformation and mitigate fracture risks. Although 316L

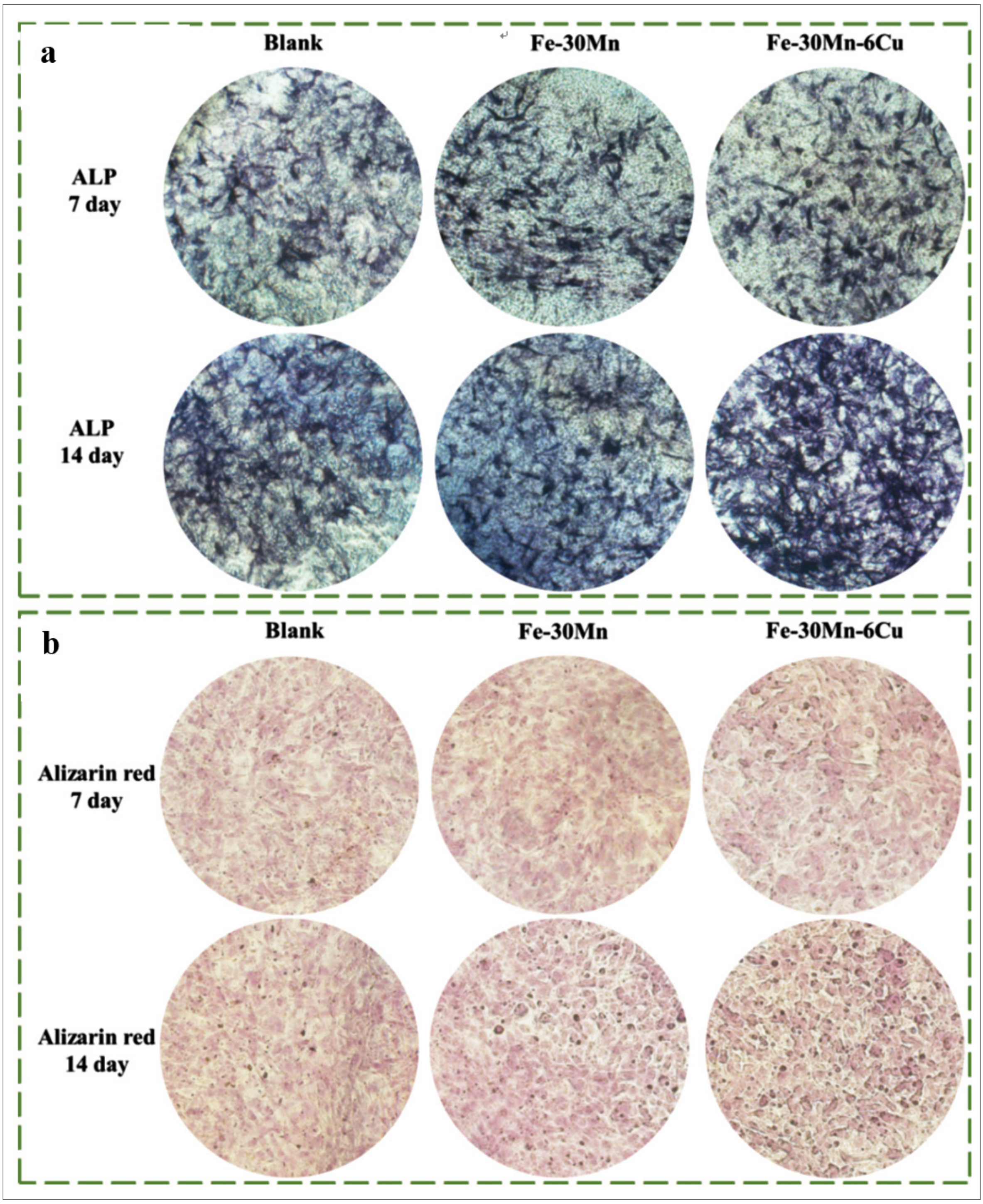

Figure 11. Osteogenic differentiation of MC3T3-E1 cells co-cultured with SLMed Fe–30Mn and SLMed Fe–30Mn–6Cu leachates. (a) Alkaline phosphatase (ALP) activity at 7 and 14 days. (b) Calcium nodule formation at 7 and 14 days.

stainless steel is widely regarded as the gold standard for orthopedic implants,[16] SLMed Fe–30Mn–6Cu exhibits comparable mechanical properties (YS: ~300 MPa; strain: ~20%) within the reported range for 316L stainless steel (YS: 50–520 MPa; strain: 8–50%).

Another key consideration for orthopedic materials is the mismatch in *E* between implant and bone, which can lead to stress shielding and subsequent implant loosening. The *E* of human bone ranges from 3 to 25 GPa,[1,16,35] substantially lower than that of 316L stainless steel. More importantly, SLMed Fe–30Mn–6Cu exhibits an *E* of ~7 GPa, aligning well with that of weight-bearing bone. Additionally, Cu alloying improved the wear resistance of the alloy, as shown in Figure 5a and b, consistent with the observed correlation between increased mechanical strength and reduced wear.[47] Given these attributes, SLMed Fe–30Mn–6Cu emerges as a promising candidate for orthopedic applications, particularly in load-bearing environments.

Magnetic resonance imaging compatibility is one of the major concerns for Fe-based biomaterials. As shown in Figure 6, SLMed Fe–30Mn and SLMed Fe–30Mn–6Cu exhibited extremely narrow magnetic hysteresis loops, reflecting their exceptionally low saturation magnetization and magnetic susceptibility. These magnetic properties are consistent with their microstructural characteristics. As previously described, SLMed Fe–30Mn comprises both the γ-austenite phase with an FCC structure and the ε-martensite phase with an HCP structure, whereas SLMed Fe–30Mn–6Cu exhibits a complete γ-austenite phase with an FCC structure.

The γ-austenite phase with an FCC structure in Fe–Mn alloys is known to be antiferromagnetic, while the ε-martensite phase with an HCP structure in Fe–Mn alloys is generally weakly magnetic or non-magnetic.[48] As a consequence, both SLMed Fe–30Mn and SLMed Fe–30Mn–6Cu are non-ferromagnetic, which supports their compatibility with MRI. From a magnetic standpoint, MRI compatibility is primarily determined by magnetic susceptibility, which is highly sensitive to the alloy's microstructure. As reported in Table 2, the magnetic susceptibility of SLMed Fe–30Mn and SLMed Fe–30Mn–6Cu decreased by two orders of magnitude compared to pure Fe (3.7×10^{-4} m^3/kg), reaching 5.25×10^{-6} and 1.33×10^{-6} m^3/kg, respectively. These values are comparable to those of widely accepted MRI-compatible 316L stainless steel.[49] To be classified as MRI-compatible of the first kind, the magnetic susceptibility of a hydrated implant material must satisfy the following condition (**Equation V**)[50]:

$$10^{-5} < |\chi - \chi_w| < 10^{-2} \qquad \text{(V)}$$

where $\chi_w = -9.05 \times 10^{-6}$ m^3/kg. MRI compatibility of the first kind implies that the material does not experience significant magnetic forces or torques when exposed to an MRI field. According to this criterion, both SLMed Fe–30Mn and SLMed Fe–30Mn–6Cu satisfy the requirements for first-kind MRI compatibility. Therefore, SLMed Fe–30Mn–6Cu—characterized by low saturation magnetization, magnetic susceptibility, and antiferromagnetic behavior—can be considered MRI-compatible. This compatibility may help mitigate MRI-related complications, such as thermal tissue damage and imaging artifacts.

4.2. Biochemical and biological properties

Biodegradable Fe-based implant materials must satisfy a wide range of functional criteria, including not only physicomechanical properties such as mechanical strength and wear resistance but also biological properties such as controlled biodegradation behavior, antibacterial efficacy, cytocompatibility, and the ability to promote osteogenic differentiation. These requirements are critical to ensure implant safety and long-term therapeutic efficacy *in vivo*.[51,52]

To address these challenges, this study developed Fe–30Mn–6Cu alloy via SLM using pure Fe, Mn, and Cu powders. The resulting material demonstrated enhanced mechanical properties, superior MRI compatibility, accelerated biodegradation, effective antibacterial activity, and excellent cytocompatibility and osteogenic differentiation in MC3T3-E1 cells. These tailored properties suggest that SLMed Fe–30Mn–6Cu can fulfill a broad spectrum of clinical requirements. However, while Fe–30Mn–6Cu shows promise as a biodegradable implant material within the Fe–Mn alloy system, its specific suitability for orthopedic applications remains unexplored. This is in contrast to the more established use of SLM-processed Fe and Fe–30Mn alloys in orthopedic contexts.

An ideal orthopedic implant material should gradually degrade after fulfilling its mechanical support role, thereby eliminating the need for a second surgery for removal.[53] Biodegradable Fe-based materials hold significant potential for orthopedic implant applications. However, a significant drawback of Fe-based alloys is their inherently slow degradation rate—intact struts have been observed even after 53 months of implantation in a porcine model.[5] This prolonged presence can impede bone regeneration and may elicit chronic inflammation or localized immune responses. Consequently, accelerating the degradation rate of Fe-based alloys has become a key focus of current research.

In this study, Fe–30Mn was developed via SLM by alloying Mn with Fe. SLMed Fe–30Mn exhibited a significantly higher biodegradation rate than its SLMed Fe counterpart.[13] This enhancement is attributed to the formation of a solid solution containing the γ-austenite phase and/or the ε-martensite phase, as evidenced by XRD analysis (Figure 3a). These phases are known to degrade more rapidly than the α-ferrite phase.[13,54]

Building upon this, Fe–30Mn–6Cu was developed by incorporating both Mn and Cu into Fe using SLM in the present work. This alloy exhibited a biodegradation rate three times greater than that of SLMed Fe–30Mn, as also reported in Table 3. This increase is primarily attributed to the presence of Cu-rich phases along grain boundaries, as confirmed by SEM imaging and EDS elemental mapping (Figures 1b and 2). These Cu-rich phases create local micro-galvanic corrosion with the matrix, thereby accelerating the biodegradation process.[55] The Cu-rich phases exhibit a much higher corrosion potential than the matrix; thus, electrons generated during matrix dissolution flow toward the Cu-rich phases (acting as cathodes), where they are consumed by dissolved O. Therefore, the anode reactions follow **Equations (VI) and (VII)**, and the cathode reaction follows **Equation (VIII)**:

$$F_e = F_e^{2+} + 2e^{-1} \tag{VI}$$

$$M_n = M_n^{2+} + 2e^{-1} \tag{VII}$$

$$2H_2O + O_2 + 4e^{-1} = 4OH^{-1} \tag{VIII}$$

A schematic representation of the anodic and cathodic reactions is illustrated in Figure 12a. Due to the local increase in pH near the Cu-rich cathodic sites, $Fe(OH)_2$ forms initially (**Equation IX**), which subsequently undergoes oxidation to $Fe(OH)_3$ (**Equation X**), as $Fe(OH)_2$ is thermodynamically unstable:

$$F_e^{2+} + 2OH^{-1} = Fe\left(OH\right)_2 \tag{IX}$$

$$4F_e\left(OH\right)_2 + O_2 + 2H_2O = 4F_e\left(OH\right)_3 \tag{X}$$

The full corrosion process is schematically illustrated in Figure 12b. This localized galvanic corrosion mechanism aligns with previous studies on metal alloys.[56] The electrochemical analysis further corroborates this behavior. As illuminated in Figure 7, SLMed Fe–30Mn–6Cu exhibited a lower value of E_{corr} and a higher value of I_{corr} compared to SLMed Fe–30Mn. These changes confirm that Cu addition enhances the degradation rate—a desirable feature for Fe-based orthopedic implants, which must degrade efficiently to prevent long-term interference with bone healing. Moreover, XPS data (Figure 3) for Fe–30Mn–6Cu confirmed the presence of Fe^{2+} species within the surface oxide layer. The presence of Fe^{2+} is significant, as it facilitates further oxidation to Fe^{3+}, thus contributing to the continued progression of degradation.

During the biodegradation process, ions are released as the Fe-based bone implant materials interact with the physiological environment. In SLMed Fe–30Mn–6Cu, Cu-rich phases contribute to the sustained release of Cu ions, which play a key role in the alloy's antibacterial activity, as depicted in Figure 9. Specifically, SLMed Fe–30Mn–6Cu exhibited a bacteriostatic rate exceeding 99% against *E. coli* and *S. aureus*.

The antimicrobial efficacy of Cu is well documented and is attributed to several mechanisms. Cu ions inhibit bacterial growth by damaging bacterial cell membranes and extracting electrons from bacterial cells, leading to oxidative damage to intracellular components, including the nucleus.[57,58] A schematic illustration of this antibacterial mechanism is provided in Figure 13.

Initially, Cu in SLMed Fe–30Mn–6Cu exists primarily in the form of Cu-rich phases. When these phases come into contact with the corrosion solution, redox reactions occur at the alloy surface, leading to the substantial release of Cu ions. These ions interact directly with bacteria adhering to the surface. Cu ions disrupt bacterial cell walls and membranes, compromise cell integrity, and interfere with metabolic processes, thereby effectively inhibiting bacterial growth.

Previous studies have demonstrated that Cu ions can extract electrons from bacteria, increasing membrane permeability and resulting in cytoplasmic leakage and oxidative damage to the cell nucleus.[59] The antibacterial performance of bone implants is essential for their clinical success, as metal surfaces can serve as attachment sites for bacteria, potentially leading to infections that delay bone healing and compromise treatment outcomes. Therefore, improving the antibacterial properties of metallic biomaterials remains a key focus in implant design. In this study, the addition of Cu to Fe–30Mn promoted the formation of Cu-rich phases that continuously released bactericidal Cu ions. These ions disrupted membrane integrity, induced cytoplasmic leakage, and facilitated oxidative damage—ultimately suppressing bacterial viability.[57,58] This sustained antibacterial effect is crucial for maintaining implant functionality in physiological environments. SLMed Fe–30Mn–6Cu thus addresses one of the major limitations of conventional Fe-based alloys—the lack of long-term antibacterial activity in clinical settings.

For iron-based materials to be clinically viable, they must be not only biodegradable and antimicrobial but also cytocompatible. Biosafety is a fundamental prerequisite in the development of medical devices. Nevertheless, during the biodegradation process, metal ions are released, and these may be cytotoxic if their concentrations exceed critical thresholds.[60] Although Fe, Mn, and Cu are essential trace elements in the human body, elevated levels can pose toxicity risks.

The challenge in developing a degradable Fe-based alloy with improved antibacterial activity lies in balancing degradation rate, antimicrobial performance, and cytocompatibility. While a higher degradation rate—such as that observed in SLMed Fe–30Mn–6Cu—enhances antimicrobial activity, it must not result in cytotoxic ion concentrations. In this work, SLMed Fe–30Mn–6Cu exhibited a threefold increase in biodegradation rate compared to its Cu-free counterpart (**Table 3**), yet maintained excellent cytocompatibility and osteogenic differentiation in MC3T3-E1 cells (Figures 10 and 11), thereby confirming its biosafety.

Furthermore, Cu addition positively influenced osteogenic activity. To assess osteogenesis, the study employed ALP activity assays and ARS staining to evaluate early-stage differentiation and mineralization, respectively. ALP is an established marker of early osteoblast differentiation, while ARS staining quantifies mineral deposition by mature osteoblasts. Experimental results demonstrated that cells treated with leachates from SLMed Fe–30Mn exhibited elevated ALP activity, indicating that Fe and Mn contributed positively to osteoblast proliferation and early differentiation. Notably, ALP activity was significantly higher in cells treated with leachates from SLMed Fe–30Mn–6Cu, indicating that Cu further promoted early-stage osteogenic differentiation. In addition, ARS staining revealed enhanced mineralization in osteoblasts exposed to SLMed Fe–30Mn–6Cu compared to SLMed Fe–30Mn, further supporting the osteoinductive role of Cu. The proposed osteogenic mechanism is illustrated in Figure 14. Cu is known to facilitate bone tissue repair by promoting osteoblast proliferation, differentiation, and matrix mineralization. Previous studies have also reported that Cu can activate osteogenic signaling pathways, thereby enhancing osteoblast function and promoting bone regeneration.[61] Therefore, this work suggests that the addition of Cu to Fe–30Mn not only improves the biodegradation rate and imparts antimicrobial properties but also supports osteogenesis, all without compromising biocompatibility.

In conjunction with its favorable physico-mechanical properties, antiferromagnetic behavior, and mechanical performance comparable to clinical gold-standard

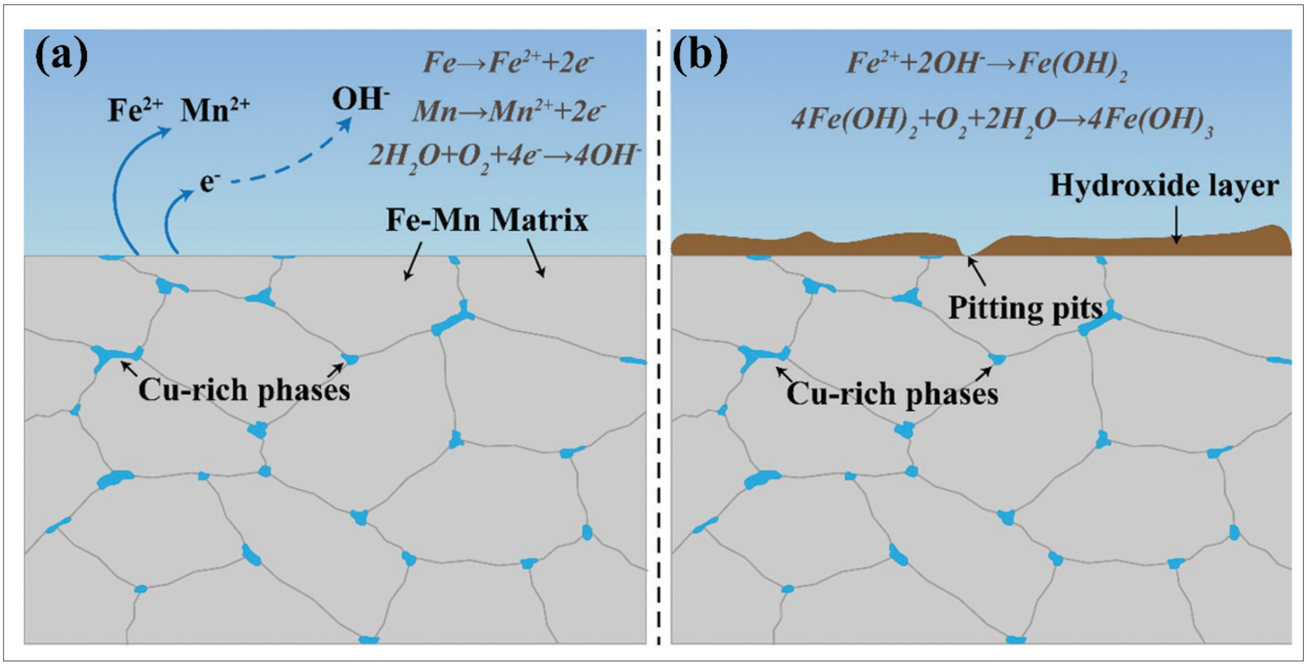

Figure 12. Schematic representation of the corrosion mechanism for SLMed Fe–30Mn–6Cu in Hank's solution.

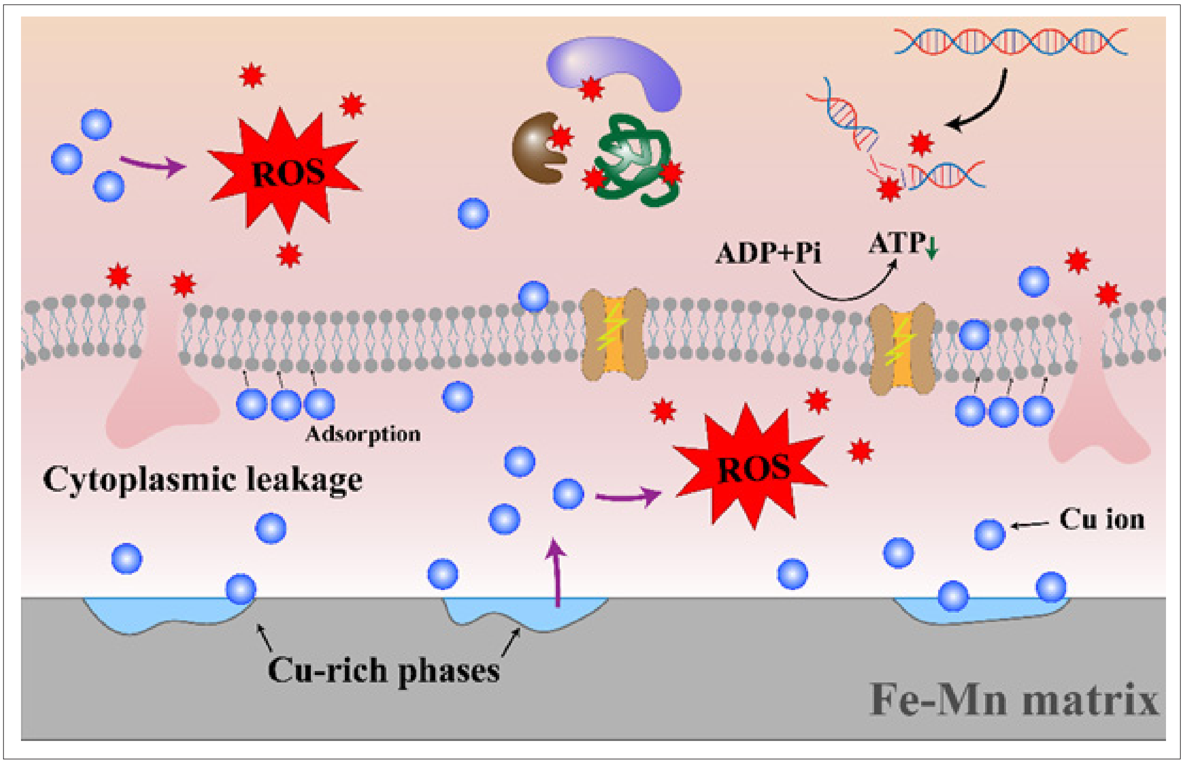

Figure 13. Schematic diagram of the antibacterial mechanism for SLMed Fe–30Mn–6Cu. Abbreviation: ROS, reactive oxygen species.

materials, SLMed Fe–30Mn–6Cu presents strong potential for orthopedic implant applications. Its integrated structure–property–function performance makes it a compelling candidate for multifunctional biomedical use. However, despite SLMed Fe–30Mn–6Cu's demonstrated advantages, the long-term *in vivo* degradation behavior and the potential accumulation of Cu ions in organs warrant further investigation. Future studies, including animal experiments, are planned to comprehensively evaluate these aspects and establish the long-term safety and efficacy of SLMed Fe–30Mn–6Cu.

5. Conclusion

In this study, a novel SLMed Fe–30Mn–6Cu alloy was developed and systematically evaluated for its suitability in orthopedic applications. The following conclusions can be drawn:

(i) Microstructural analysis revealed that SLMed Fe–30Mn–6Cu exhibited a complete γ-austenite phase microstructure, characterized by fine equiaxed grains (~7 μm) and the presence of Cu-enriched intergranular second-phase particles.

(ii) Compared to the SLMed Fe–30Mn alloy, the SLMed Fe–30Mn–6Cu presented a ~24% increase in YS, reaching ~230 MPa. Additionally, it showed improved wear resistance, reduced hysteresis loop area—indicative of MRI compatibility—and a biodegradation rate three times higher.

(iii) The mechanical properties of the SLMed Fe–30Mn–6Cu alloy approached those of 316L stainless steel, while the *E* value (~32 GPa) remained within the range of human weight-bearing bones.

(iv) The SLMed Fe–30Mn–6Cu demonstrated strong antibacterial activity, with bacteriostatic rates exceeding 99% against *E. coli* and *S. aureus*. It also demonstrated excellent cytocompatibility and promoted osteogenic differentiation in MC3T3-E1 cells.

(v) Overall, the SLMed Fe–30Mn–6Cu alloy exhibited multifunctional superiority, including suitable physicomechanical properties, accelerated biodegradation, potent antibacterial efficacy, and favorable biological responses (i.e., cytocompatibility and osteogenic differentiation). These findings suggest that the alloy holds significant promise as a next-generation material for orthopedic applications, offering a high degree of structure–property–function integration.

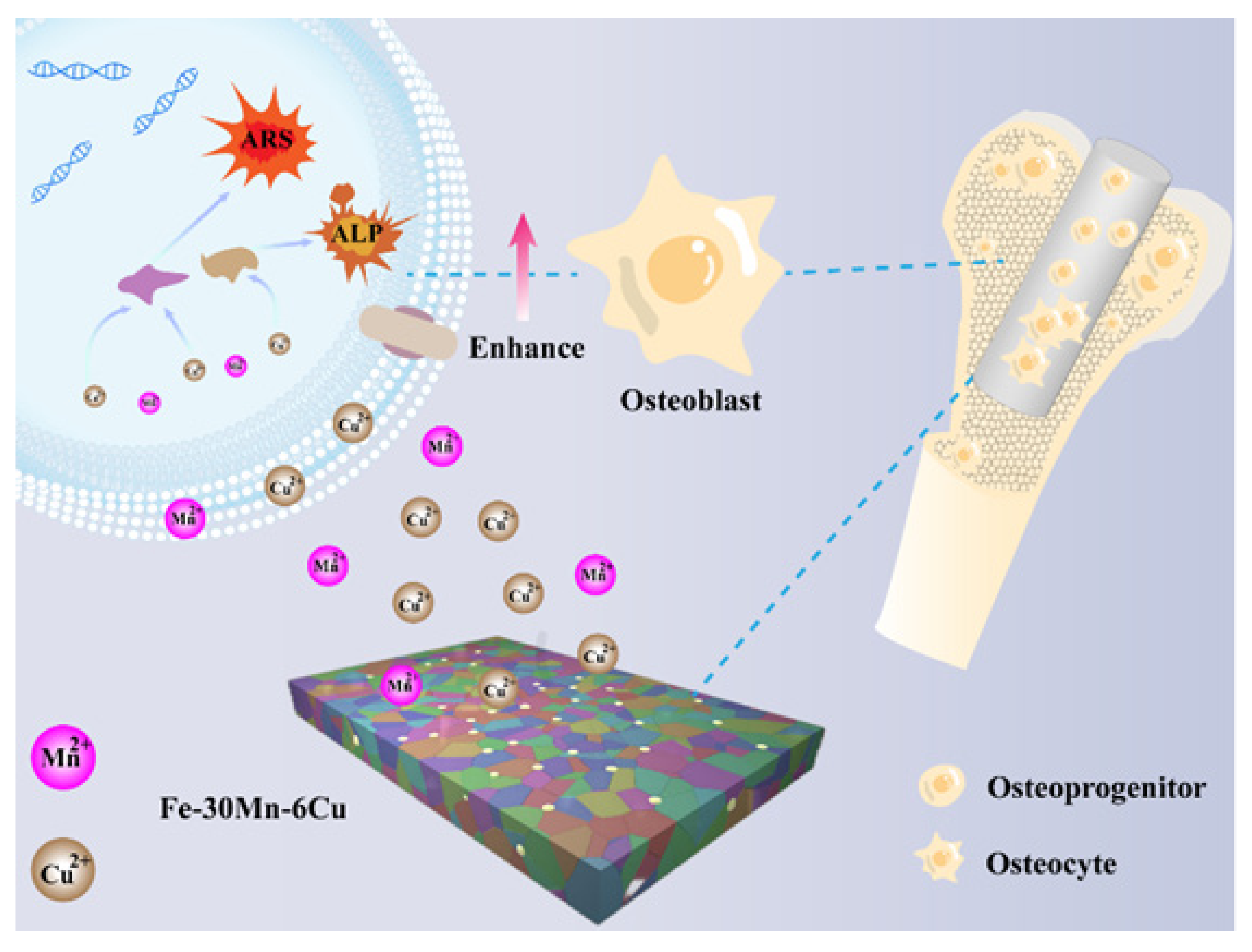

Figure 14. Schematic diagram of the osteogenic mechanism for SLMed Fe–30Mn–6Cu.

Acknowledgments

None.

Funding

The study was financially supported by the National Natural Science Foundation of China (No. 52305313), the Natural Science Foundation of Hunan Province (No. 2023JJ40553), and the Natural Science Foundation of Shandong Province (No. ZR2023ME181).

Conflict of interest

The authors declare they have no conflict of interest.

Author contributions

Conceptualization: Ming-Chun Zhao
Formal analysis: Yingchao Zhao, Junjie Cheng, Xin Li
Investigation: Xinjun Yang, Guanping Chen, Yingchao Zhao
Methodology: Xin Li, Xinhong Yin, Yali He
Writing–original draft: Xinjun Yang
Writing–review & editing: Ming-Chun Zhao

Ethics approval and consent to participate

Not applicable.

Consent for publication

Not applicable.

Availability of data

All data included in this study are available upon request by contact with the corresponding author.

References

1. Liu Z, Zhao MC, Yin D, Zhao YC, Atrens A. Bio-functional niobium-based metallic biomaterials: Exploring their physicomechanical properties, biological significance, and implant applications. *Acta Biomater*. 2025;192:1-27. doi: 10.1016/j.actbio.2024.12.036
2. Zhang Y, Roux C, Rouchaud A, et al. Recent advances in Fe-based bioresorbable stents: materials design and biosafety. *Bioact Mater*. 2023;31:333-354. doi: 10.1016/j.bioactmat.2023.07.024
3. Putra NE, Leeflang MA, Minneboo M, et al. Extrusion-based 3D printed biodegradable porous iron. *Acta Biomater*. 2021;121:741-756. doi: 10.1016/j.actbio.2020.11.022
4. Li Y, Jahr H, Lietaert K, et al. Additively manufactured biodegradable porous iron. *Acta Biomater*. 2018; 77:380-393. doi: 10.1016/j.actbio.2019.10.034
5. Lin W, Qin L, Qi H, et al. Long-term in vivo corrosion behavior, biocompatibility and bioresorption mechanism of a bioresorbable nitrided iron scaffold. *Acta Biomater*. 2017;54:454-468. doi: 10.1016/j.actbio.2017.03.020
6. Zhao Y, Feng J, Yu H, et al. Comparative study on biodegradation of pure iron prepared by microwave sintering and laser melting. *Materials (Basel)*. 2022; 15(4):1604. doi: 10.3390/ma15041604
7. Liu B, Zheng YF. Effects of alloying elements (Mn, Co, Al, W, Sn, B, C and S) on biodegradability and in vitro biocompatibility of pure iron. *Acta Biomater*. 2011;7(3):1407-1420. doi: 10.1016/j.actbio.2010.11.001
8. Li S, Ren J, Wang X, et al. Dilemmas and countermeasures of Fe-based biomaterials for next-generation bone implants. *J Mater Res Technol*. 2022;20:2034-2050. doi: 10.1016/j.jmrt.2022.07.089
9. Putra NE, Leeflang MA, Taheri P, et al. Extrusion-based 3D printing of ex situ -alloyed highly biodegradable MRI-friendly porous iron-manganese scaffolds. *Acta Biomater*. 2021;134:774-790. doi: 10.1016/j.actbio.2021.07.042
10. He J, He F-L, Li D-W, et al. Advances in Fe-based biodegradable metallic materials. *RSC Adv*. 2016;6:112819-112838. doi: 10.1039/c6ra20594a
11. Filli L, Luechinger R, Frauenfelder T, et al. Metal-induced artifacts in computed tomography and magnetic resonance imaging: comparison of a biodegradable magnesium alloy versus titanium and stainless steel controls. *Skeletal Radiol*. 2015;44(6):849-856. doi: 10.1007/s00256-014-2057-5
12. Campoccia D, Montanaro L, Arciola CR. The significance of infection related to orthopedic devices and issues of antibiotic resistance. *Biomaterials*. 2006;27(11):2331-2339. doi: 10.1016/j.biomaterials.2005.11.044
13. Guo Y, Zhao M, Xie B, et al. In vitro corrosion resistance and antibacterial performance of novel Fe-xCu biomedical alloys prepared by selective laser melting. *Adv Eng Mater*. 2021;23:2001000. doi: 10.1002/adem.202001000
14. Cordova LA, Stresing V, Gobin B, et al. Orthopaedic implant failure: aseptic implant loosening--the contribution and future challenges of mouse models in translational research. *Clin Sci (Lond)*. 2014;127(5):277-293. doi: 10.1042/CS20130338
15. Li X, Zhao YC, Yin D, et al. Microwave-sintered nano-SiC reinforced 8SiC/Ti-3Cu composite: fabrication, wear resistance, antibacterial function, and biocompatibility. *Adv Healthc Mater*. 2025;14(6):e2403626. doi: 10.1002/adhm.202403626
16. Hermawan H, Purnama A, Dube D, Couet J, Mantovani D. Fe-Mn alloys for metallic biodegradable stents: degradation and cell viability studies. *Acta Biomater*. 2010;6(5):1852-1860. doi: 10.1016/j.actbio.2009.11.025
17. Liu P, Huang Q, Shan Q, et al. Achieving exceptional work-hardening capability of additively-manufactured multiphase Fe-Mn alloys via multiple deformation mechanisms, *Int J Plast*. 2024;173:103871. doi: 10.1016/j.ijplas.2023.103871
18. Schinhammer M, Haenzi AC, Loeffler JF, Uggowitzer PJ. Design strategy for biodegradable Fe-based alloys for medical applications. *Acta Biomater*. 2010;6:1705-1713. doi: 10.1016/j.actbio.2009.07.039
19. Li JL, Zhao MC, Zhao YC, et al. Customization and prospects of friction stirprocessing for improving the biomedicalproperties of metallic implants fororthopedic applications. *J Mater Res Technol*. 2025;34:2133-2149. doi: 10.1016/j.jmrt.2024.12.191
20. Mandal S, Viraj, Nandi SK, Roy M. Effects of multiscale porosity and pore interconnectivity on in vitro and in vivo degradation and biocompatibility of Fe–Mn–Cu scaffolds. *J Mater Chem B*. 2021;9:4340-4354. doi: 10.1039/D1TB00641J
21. Zhao Y, Tang Y, Zhao M, et al. Graphene oxide reinforced iron matrix composite with enhanced biodegradation rate prepared by selective laser melting. *Adv Eng Mater*. 2019;21:1900314. doi: 10.1002/adem.201900314
22. Zhao YC, Tang Y, Zhao MC, et al. Study on Fe-xGO composites prepared by selective laser melting: microstructure, hardness, biodegradation and cytocompatibility. *JOM* 2020;72: 1163-1174 (2020). doi: 10.1007/s11837-019-03814-z

23. Zhao, MC., Zhao, YC., Yin, DF. *et al.* Biodegradation behavior of coated as-extruded Mg–Sr alloy in simulated body fluid. *Acta Metall Sin. (Engl Lett.)* 2019;32:1195-1206.
doi: 10.1007/s40195-019-00892-5

24. Cherqaoui A, Cao QN, Gatto ML, Paternoster C, Mengucci P, Mantovani D. Degradation behavior of austenite, ferrite, and martensite present in biodegradable Fe-based alloys in three protein-rich pseudo-physiological solutions. *Bioact Mater*. 2024;41:96-107.
doi: 10.1016/j.bioactmat.2024.06.025

25. Dargusch MS, Venezuela J, Dehghan-Manshadi A, et al. In vivo evaluation of bioabsorbable Fe-35Mn-1Ag: first reports on in vivo hydrogen gas evolution in Fe-based implants. *Adv Healthc Mater*. 2021;10(2):e2000667.
doi: 10.1002/adhm.202000667

26. Ren G, Huang L, Hu K, et al. Enhanced antibacterial behavior of a novel Cu-bearing high-entropy alloy. *J Mater Sci Technol*. 2022;117:158-166.
doi: 10.1016/j.jmst.2022.02.001

27. Yan X, Wan P, Tan L, Zao M, Shuai C, Yang K. Influence of hybrid extrusion and solution treatment on the microstructure and degradation behavior of Mg-0.1Cu alloy. *Mater Sci Eng: B*. 2018;229:105-117.
doi: 10.1016/j.mseb.2017.12.033

28. Goudarzi P, Moazami-Goudarzi M, Masoudi A. Sintering, microstructure and properties of absorbable Fe–Mn-xCu alloys. *Mater Chem Phys*. 2022;287:126368.
doi: 10.1016/j.matchemphys.2022.126368

29. Zhao Y, Cao Y, Wen W, et al. Effects of Mn content on austenite stability and mechanical properties of low Ni alumina-forming austenitic heat-resistant steel: a first-principles study. *Sci Rep*. 2023;13(1):5769.
doi: 10.1038/s41598-023-32968-9

30. Martínez J, Cotes SM, Cabrera AF, Desimoni J, Fernández Guillermet A. On the relative fraction of ε martensite in γ-Fe–Mn alloys. *Mater Sci Eng A*. 2005;408:26-32.
doi: 10.1016/j.msea.2005.06.019

31. Dargusch MS, Dehghan-Manshadi A, Shahbazi M, et al. Exploring the role of manganese on the microstructure, mechanical properties, biodegradability, and biocompatibility of porous iron-based scaffolds. *ACS Biomater Sci Eng*. 2019;5(4):1686-1702.
doi: 10.1021/acsbiomaterials.8b01497

32. Xie B, Zhao M-C, Tao J-X, et al. Comparison of the biodegradation of ZK30 subjected to solid solution treating and selective laser melting. *J Mater Res Technol*. 2021;10:722-729.
doi: 10.1016/j.jmrt.2020.12.041

33. Ji H, Zhao M-C, Xie B, et al. Corrosion and antibacterial performance of novel selective-laser-melted (SLMed) Ti-xCu biomedical alloys. *J Alloys Compd*. 2021;864:158415.
doi: 10.1016/j.jallcom.2020.158415

34. Wu S, Liu X, Yeung KWK, Liu C, Yang X. Biomimetic porous scaffolds for bone tissue engineering. *Mater Sci Eng Rep*. 2014;80:1–36.
doi: 10.1016/j.mser.2014.04.001

35. Wu M, Zhao M, Cai Y, Yao J, Wang P, Atrens A. Recent advances in bio-functional Ta-based bone materials: materials design and bioactivity. *Int J Extrem Manuf*. 2024;6:062010.
doi: 10.1088/2631-7990/ad7b03

36. Ryan G, Pandit A, Apatsidis DP. Fabrication methods of porous metals for use in orthopaedic applications. *Biomaterials*. 2006;27:2651-2670.
doi: 10.1016/j.biomaterials.2005.12.002

37. Zhang W, Tan L, Ni D, et al. Effect of grain refinement and crystallographic texture produced by friction stir processing on the biodegradation behavior of a Mg-Nd-Zn alloy. *J Mater Sci Technol*. 2019;35(5):777-783.
doi: 10.1016/j.jmst.2018.11.025

38. Song Z, Cai Y, Li X, et al. Fresh insights into structure–function-integrated self-antibacterial Cu-containing Al alloys: giving Al alloys a new function. *Mater Horiz*. 2025;12:814-832.
doi: 10.1039/D4MH00770K

39. Wang KX, Yin D, Zhao Y, Atrens A, Zhao M. Microstructural evolution upon heat treatments and its effect on corrosion in Al-Zn-Mg alloys containing Sc and Zr. *J Mater Res Technol*. 2020;9:5077-5089.
doi: 10.1016/j.jallcom.2022.168001

40. Liu P, Wu H, Liang L, et al. Microstructure, mechanical properties and corrosion behavior of additively-manufactured Fe–Mn alloys. *Mater Sci Eng A*. 2022;852:143585.
doi: 10.1016/j.msea.2022.143585

41. Bhadeshia H, Honeycombe R. Chapter 4 - Solutes that substitute for iron. In: Bhadeshia H, Honeycombe R (eds.). Steels: Microstructure and Properties, Fourth Edition, Butterworth-Heinemann; 2017:101-134.
doi: 10.1016/B978-0-08-100270-4.00004-4

42. Bairagi D, Mandal S. A comprehensive review on biocompatible Mg-based alloys as temporary orthopaedic implants: current status, challenges, and future prospects. *J Magn Alloys*. 2022;10:627-669.
doi: 10.1016/j.jma.2021.09.005

43. Wang X, Xu S, Zhou S, et al. Topological design and additive manufacturing of porous metals for bone scaffolds and orthopaedic implants: a review. *Biomaterials*. 2016;83:127-141.
doi: 10.1016/j.biomaterials.2016.01.012

44. Heiden M, Nauman E, Stanciu L. Bioresorbable Fe-Mn and Fe-Mn-HA materials for orthopedic implantation: enhancing degradation through porosity control. *Adv Healthc Mater*. 2017;6(13):1700120.
doi: 10.1002/adhm.201700120

45. Hermawan H, Dubé D, Mantovani D. Development of degradable Fe-35Mn alloy for biomedical application. *Adv Mater Res*. 2006;15–17:107-112.
doi: 10.4028/www.scientific.net/AMR.15-17.107

46. Mandal S, Kishore AV, Mandal S, et al. Controlled nano Cu precipitation through age treatment: a method to enhance the biodegradation, mechanical, antimicrobial properties and biocompatibility of Fe-20Mn-3Cu alloys. *Acta Biomater*. 2023;168:650-669.
doi: 10.1016/j.actbio.2023.07.004

47. Lu X, Zhang D, Xu W, et al. The effect of Cu content on corrosion, wear and tribocorrosion resistance of Ti-Mo-Cu alloy for load-bearing bone implants. *Corros Sci*. 2020;177:109007.
doi: 10.1016/j.corsci.2020.109007

48. Lintzen S, von Appen J, Hallstedt B, Dronskowski R. The Fe–Mn enthalpy phase diagram from first principles. *J Alloys Compd*. 2013;577:370-375.
doi: 10.1016/j.jallcom.2013.06.006

49. Jurgeleit T, Quandt E, Zamponi C. Magnetron sputtering as a fabrication method for a biodegradable Fe32Mn alloy. *Materials (Basel)*. 2017;10(10):1196.
doi: 10.3390/ma10101196

50. Schenck JF. The role of magnetic susceptibility in magnetic resonance imaging: MRI magnetic compatibility of the first and second kinds. *Med Phys*. 1996;23:815-850.
doi: 10.1118/1.597854

51. Lee MK, Lee H, Park C, et al. Accelerated biodegradation of iron-based implants via tantalum-implanted surface nanostructures. *Bioact Mater*. 2021;9:239-250.
doi: 10.1016/j.bioactmat.2021.07.003

52. Wang P, Wang Q, Wu D, et al. Enhancing osteogenic bioactivities of coaxial electrospinning nano-scaffolds through incorporating iron oxide nanoparticles and icaritin for bone regeneration. *Nano Res.* 2024;17:6430-6442.
doi: 10.1007/s12274-024-6656-8

53. Gao YN, Yang HT, Qiu ZF, et al. Long-term efficacy, safety and biocompatibility of a novel sirolimus eluting iron bioresorbable scaffold in a porcine model. *Bioact Mater*. 2024;39:135-146.
doi: 10.1016/j.bioactmat.2024.05.027

54. Liu B, Zheng YF, Ruan L. In vitro investigation of Fe30Mn6Si shape memory alloy as a potential biodegradable metallic material. *Mater Lett*. 2011; 65:540-543.
doi: 10.1016/j.matlet.2010.10.068

55. Zhang W, Zao MC, Wang Z, et al. Enhanced initial biodegradation resistance of the biomedical Mg-Cu alloy by surface nanomodification. *J Magnes Alloys*. 2023;11:2776-2788.
doi: 10.1016/j.jma.2021.12.013

56. Venezuela J, Dargusch MS. Addressing the slow corrosion rate of biodegradable Fe-Mn: current approaches and future trends. *Curr Opin Solid State Mater Sci*. 2020; 24:100822.
doi: 10.1016/j.cossms.2020.100822

57. Godoy-Gallardo M, Eckhard U, Delgado LM, et al. Antibacterial approaches in tissue engineering using metal ions and nanoparticles: from mechanisms to applications. *Bioact Mater*. 2021;6:4470-4490.
doi: 10.1016/j.bioactmat.2021.04.033

58. Zhang E, Zao X, Hu J, Wang R, Fu S, Qin G. Antibacterial metals and alloys for potential biomedical implants. *Bioact Mater*. 2021;6:2569-2612.
doi: 10.1016/j.bioactmat.2021.01.033

59. Nan L, Liu Y, Lü M, Yang K. Study on antibacterial mechanism of copper-bearing austenitic antibacterial stainless steel by atomic force microscopy. *J Mater Sci Matern Med*. 2008;19:3057-3062.
doi: 10.1016/j.bioactmat.2021.01.030

60. Zheng YF, Gu XN, Witte F. Biodegradable metals. *Mater Sci Eng R: Rep*. 2014;77:1–34.
doi: 10.1016/j.mser.2014.01.001

61. Yuan Y, Jin S, Qi X, et al. Osteogenesis stimulation by copper-containing 316L stainless steel via activation of akt cell signaling pathway and Runx2 upregulation. *J Mater Sci Technol*. 2019;35:2727-2733.
doi: 10.1016/j.jmst.2019.04.028